Sierra Barrier Jets, Atmospheric Rivers, and Precipitation Characteristics in Northern California: A Composite Perspective Based on a Network of Wind Profilers

PAUL J. NEIMAN

Physical Sciences Division, NOAA/Earth System Research Laboratory, Boulder, Colorado

MIMI HUGHES AND BENJAMIN J. MOORE

Cooperative Institute for Research in the Environmental Sciences, and NOAA/Earth System Research Laboratory, Boulder, Colorado

F. MARTIN RALPH

Physical Sciences Division, NOAA/Earth System Research Laboratory, Boulder, Colorado

ELLEN M. SUKOVICH

Cooperative Institute for Research in the Environmental Sciences, and NOAA/Earth System Research Laboratory, Boulder, Colorado

(Manuscript received 1 April 2013, in final form 8 July 2013)

ABSTRACT

Five 915-MHz wind profilers and GPS receivers across California's northern Central Valley (CV) and adjacent Sierra foothills and coastal zone, in tandem with a 6-km-resolution gridded reanalysis dataset generated from the Weather Research and Forecasting Model, document key spatiotemporal characteristics of Sierra barrier jets (SBJs), landfalling atmospheric rivers (ARs), and their interactions. Composite kinematic and thermodynamic analyses are based on the 13 strongest SBJ cases observed by the Sloughhouse profiler between 2009 and 2011. The analyses show shallow, cool, south-southeasterly (i.e., Sierra parallel) flow and associated water vapor transport strengthening with time early in the 24-h compositing period, culminating in an SBJ core at <1 km above ground over the eastern CV. The SBJ core increases in altitude up the Sierra's windward slope and poleward toward the north end of the CV, but it does not reach the westernmost CV. Above the developing SBJ, strengthening southwesterly flow descends temporally in response to the landfalling AR. The moistening SBJ reaches maximum intensity during the strongest AR flow aloft, at which time the core of the AR-parallel vapor transport slopes over the SBJ. The inland penetration of the AR through the San Francisco Bay gap in the coastal mountains contributes to SBJ moistening and deepening. The SBJ subsequently weakens with the initial cold-frontal period aloft, during which the shallow flow shifts to southwesterly and the heaviest precipitation falls in the Sierra foothills. An orographic precipitation analysis quantitatively links the Sierra-perpendicular (nearly AR parallel) vapor fluxes to enhanced precipitation along the Sierra's windward slope and the SBJ-parallel fluxes to heavy precipitation at the north end of the CV.

1. Introduction

The mountains of Northern California, including the prominent Sierra Nevada, play a key role in the generation of orographically enhanced heavy precipitation during landfalling winter storms (e.g., Heggli and Rauber 1988; Pandey et al. 1999; Dettinger et al. 2004). Much of the precipitation is captured as snowmelt by large reservoirs and provides water and hydroelectric power to many of the ~38 million residents of California (see descriptions of the Central Valley Project and State Water Project at www.usbr.gov/mp/cvp and www.water.ca.gov/swp), the nation's most populous state. Because of the frequent occurrence of heavy orographic precipitation in Northern California, the region is also susceptible to devastating flooding (e.g., Dettinger et al. 2012). In fact, the state's capital, Sacramento, is recognized as one of the most

Corresponding author address: Paul J. Neiman, Physical Sciences Division, NOAA/Earth System Research Laboratory, Mail Code R/PSD2; 325 Broadway, Boulder, CO 80305.
E-mail: paul.j.neiman@noaa.gov

DOI: 10.1175/MWR-D-13-00112.1

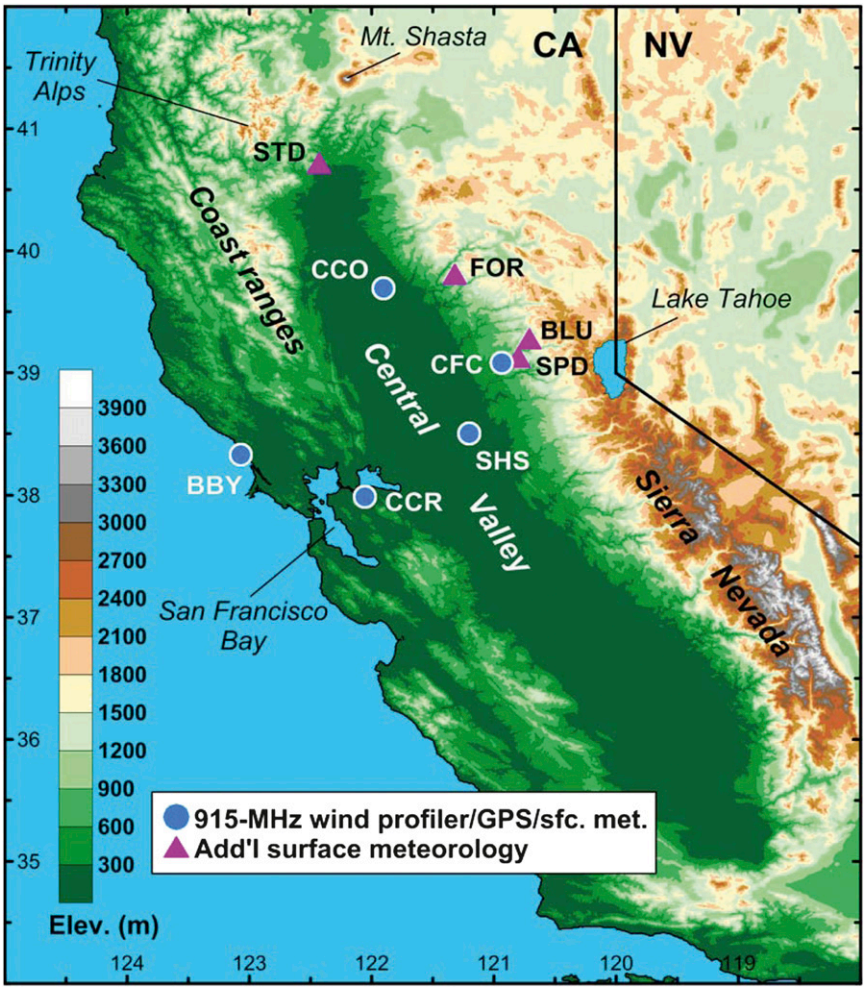

FIG. 1. Terrain base map of California showing the locations of five 915-MHz wind profilers (blue circles) and four surface meteorological stations (purple triangles).

vulnerable cities in America to the ravages of catastrophic flooding (e.g., Lund 2007). Two meteorological phenomena, and their interactions, significantly modulate the precipitation that falls across interior Northern California: terrain-locked Sierra barrier jets (SBJs) above the western slope of the Sierra and landfalling atmospheric rivers (ARs).

SBJs were first documented during the Sierra Cooperative Pilot Project (SCPP; Reynolds and Dennis 1986) and subsequently reported on in airborne-centric case studies (Parish 1982; Marwitz 1983, 1987) and in a multiwinter compositing study using 1849 rawinsondes launched from the windward base of the Sierra (Smutz 1986). Recent research expands upon these earlier findings and highlights the importance of the SBJ in modulating precipitation distributions across Northern California. Galewsky and Sobel (2005) used a mesoscale model to show that an SBJ acted as a dynamic barrier along the windward slope of the northern Sierra and contributed to flooding rains there. Kim and Kang (2007) employed climate simulations during a winter season, and Smith et al. (2010) used a mesoscale model for a case study to document the role of SBJs in transporting water vapor poleward toward the north end of California's Central Valley (CV; see Fig. 1), with a concomitant enhancement in precipitation there. Lundquist et al. (2010) found that the observed orographic precipitation gradient up the Sierra's windward slope is inversely proportional to observed SBJ height.

SBJs form in response to the deceleration of stably stratified flow as it approaches the western Sierra foothills. The flow turns leftward toward the north end of the CV in response to a weakened Coriolis force when the Froude number ($F_r = U/Nh$, where U is the incoming flow, N is the Brunt–Väisälä frequency, and h is terrain height) is between 0 and 1 (Pierrehumbert and Wyman 1985; Smolarkiewicz and Rotunno 1990). The resulting corridor of blocked flow, which is maintained in

conjunction with a statically stable pressure ridge dammed against the Sierra's windward slope, parallels the range's long axis on its west side below crest level. Similar barrier jet flows have been documented along the windward slope of prominent mountain ranges across North America (e.g., Bell and Bosart 1988; Colle and Mass 1995; Loescher et al. 2006; Braun et al. 1997; Yu and Smull 2000) and elsewhere around the world.

The multiyear wind profiler compositing study by Neiman et al. (2010) demonstrates that the strongest SBJs occur in a stably stratified, pre-cold-frontal environment during the baroclinically active cool season (October–April) and are typically associated with the heaviest precipitation events and with landfalling ARs. Atmospheric rivers are long (greater than ~2000 km), narrow (less than ~1000 km), low-level (below ~600 hPa) plumes of enhanced water vapor flux (e.g., Zhu and Newell 1998; Ralph et al. 2004; Neiman et al. 2008b, 2011; Smith et al. 2010) embedded within a broader region of generally poleward heat transport in the warm sector of extratropical cyclones. Because ARs are often accompanied by strong, moist, and warm low-level onshore flow with high melting levels, they frequently contribute to heavy orographic precipitation, flooding, and high-altitude snowpack replenishment along the topographically complex west coasts of continents (e.g., Dettinger 2004; Ralph et al. 2006, 2011; Stohl et al. 2008; Neiman et al. 2008a,b, 2011; Viale and Nuñez 2011; Lavers et al. 2011; Dettinger et al. 2011; Guan et al. 2012; Ralph and Dettinger 2012), including in the Sierra Nevada.

The interaction between SBJs and landfalling ARs was first addressed in the observation-based case study by Kingsmill et al. (2013). They used a suite of scanning and profiling Doppler radars, global positioning system (GPS) receivers, and serial rawinsondes to document the kinematic and thermodynamic structures of a pair of SBJs and ARs across the northern CV and up the western Sierra slope. Our study, which utilizes five wind profilers in Northern California as observational anchors (see Fig. 1), extends this earlier research by examining the composite evolution of SBJs, ARs, and their interactions during many events over multiple years. In addition, unlike the Kingsmill et al. (2013) study or the ones preceding it, we quantify the temporal and orographic linkages between SBJs, ARs, and the precipitation they generate across the northern CV and Sierra foothills. Finally, our study analyzes a unique finescale (6-km horizontal resolution) regional downscaling of reanalysis data (Hughes et al. 2012), which was created specifically to study SBJs, in conjunction with the wind profiler data to obtain a more complete kinematic and thermodynamic depiction of the composite SBJ and AR evolutions.

2. Observing systems and gridded datasets

Research data were collected from a suite of five 915-MHz radar wind profilers (e.g., Carter et al. 1995) in California's CV and coastal zone: Sloughhouse (SHS), Colfax (CFC), Chico (CCO), Concord (CCR), and Bodega Bay (BBY) (Fig. 1, Table 1). The profilers, which use a steerable three-beam system to detect the Doppler shift of horizontal and vertical air motions, were deployed by the National Oceanic and Atmospheric Administration's Earth System Research Laboratory (NOAA/ESRL) in support of NOAA's Hydrometeorology Testbed (HMT; http://hmt.noaa.gov/) program (Ralph et al. 2005) and the California Energy Commission's CalWater project (www.esrl.noaa.gov/psd/calwater/), and they represent the observational foundation of this study. The analysis presented in this study is predicated on the availability of wind profiler data collected at SHS because of its proximity to the HMT's domain of primary interest in the American River basin area. The profiler operated for six cool seasons (i.e., November into April) between 2005 and 2011 (Table 1). Concurrent data were collected at the other profilers for the same, or fewer, number of cool seasons (Table 1). The profilers provided hourly averaged vertical profiles of horizontal wind velocity from ~0.1 to 4.0 km above ground with ~100-m vertical resolution and ~1 $m\,s^{-1}$ accuracy. The winds were edited objectively using the vertical–temporal continuity method of Weber et al. (1993), and an extra level of quality control was performed by visual inspection to flag the few remaining outliers.

A dual-channel GPS receiver at each wind profiler site provided 30-min measurements of integrated water vapor (IWV) in the full atmospheric column with ~1 mm accuracy by measuring delays in the arrival of radio signals transmitted by the constellation of GPS satellites (Duan et al. 1996; Mattioli et al. 2007). Each profiler site, as well as two additional sites on the windward slope of the Sierra [Sugar Pine Dam (SPD) and Blue Canyon (BLU)] and a third at the northern end of the CV [Shasta Dam (STD)], featured a 10-m tower that measured standard surface meteorological parameters, including precipitation, every 2 min. Hourly data from two additional precipitation gauges [Four Trees (FOR) and Blue Canyon (BLC, used to replace the comparatively poor-quality precipitation data at BLU)] were acquired from the California Data Exchange Center (http://cdec.water.ca.gov). The time interval between measurements ranged from 15 to 60 min, depending on the precipitation intensity, while the minimum measurement resolution was 0.04 inches (i.e., 1.016 mm). See Table 1 and Fig. 1 for a list of GPS and surface sites, their locations, and data outages.

TABLE 1. Site information and data availability for the study's key observing platforms in California. See Table 2 for the date range of each SBJ case number. Surface meteorological sites (sfc met) include a precipitation gauge.

Location	Three-letter name	Instrument	Lat. (°N)	Lon. (°W)	Altitude (m MSL)	Wind profiler operating periods	Data outages for 13-case composites
Sloughhouse	SHS	Wind profiler, GPS, sfc met	38.50	121.21	50	15 Dec 2005–18 Apr 2006 1 Dec 2006–28 Mar 2007 30 Nov 2007–11 Apr 2008 21 Nov 2008–27 Apr 2009 18 Nov 2009–26 Apr 2010 4 Nov 2010–22 Mar 2011	Case 11: no IWV
Colfax	CFC	Wind profiler, GPS, sfc met	39.08	120.94	644	19 Nov 2008–12 May 2009 27 Oct 2009–25 Apr 2010 3 Nov 2010–22 Mar 2011	Case 17: partial IWV
Chico	CCO	Wind profiler, GPS, sfc met	39.69	121.91	41	1 Jan 2005–22 Mar 2011	
Concord	CCR	Wind profiler, GPS, sfc met	37.99	122.06	14	2 Dec 2009–28 Apr 2010 19 Nov 2010–21 Mar 2011	Cases 11–14: no IWV
Bodega Bay	BBY	Wind profiler, GPS, sfc met	38.32	123.07	12	1 Jan 2005–22 Mar 2011	
Sugar Pine Dam	SPD	GPS, sfc met	39.13	120.80	1066		
Blue Canyon	BLU	Sfc met	39.28	120.71	1610		
Four Trees	FOR	Precipitation gauge	39.81	121.32	1570		
Shasta Dam	STD	Sfc met	40.72	122.43	183		

Precipitation analyses were generated from NOAA's National Centers for Environmental Prediction (NCEP) Stage IV multisensor precipitation dataset (Baldwin and Mitchell 1997; Fulton et al. 1998), which is on a 4-km grid and is available in real time every hour and 6 h from NOAA's 12 River Forecast Centers (RFCs) across the continental United States. In the Intermountain West, the analyses are created by distributing the precipitation gauge data onto the grid using mountain mapper (e.g., Schaake et al. 2004), which uses the climatologically based Parameter-Elevation Regressions on Independent Slopes Model (PRISM; Daly et al. 1994). The grids are subjected to manual quality control at the RFCs. The Stage IV analysis includes 1-, 6-, and 24-h precipitation accumulations; the 6-h accumulations are used here.

This study utilizes the North American Regional Reanalysis (NARR) gridded dataset (Mesinger et al. 2006). Covering North America and adjacent oceans, the NARR is available from 1979 to present with a horizontal grid spacing of 32 km and 45 vertical levels at 3-h intervals. In addition, we use a finer-scale gridded dataset described in an 11-yr SBJ validation study by Hughes et al. (2012). In that study, the NARR was dynamically downscaled with the Weather Research and Forecasting Model (WRF) [WRF reanalysis downscaling (WRF-RD)]. The downscaled simulation contains an 18-km horizontal resolution outer domain across California and the eastern Pacific and a two-way nested 6-km inner domain covering only California. Both resolutions are available hourly. At 6-km horizontal resolution, the major mountain complexes in California are resolved. Each domain contains 27 vertical levels, with the finest vertical resolution relegated to the lower troposphere.

3. Case selection and compositing methodologies

Using the methodology in Neiman et al. (2010), our study objectively tags SBJ cases observed by the SHS profiler during its six cool seasons of deployment between 2005/06 and 2010/11. Specifically, an individual hourly averaged wind profile must have a relative maximum in the Sierra-parallel component of the flow (V, directed from 160°) of greater than 12 m s^{-1} below 3 km MSL (i.e., below crest level). If more than one relative maximum is observed, the maximum with the greatest V is taken as the SBJ in that profile (V_{maxprof}). Also, V has to decrease by more than 2 m s^{-1} between the altitude of V_{maxprof} and 3 km MSL. Furthermore, V_{maxprof} must occur at or above the second profiler range gate (i.e., $\geq\sim$200 m above ground) to eliminate shallow surface-based flows, and range gates adjacent in altitude to V_{maxprof} must contain data. These criteria ensure that only those profiles exhibiting an unambiguous SBJ signature are included in the subsequent analyses. Finally, SBJ ''cases'' are composed of at least eight consecutive hourly profiles fulfilling the above criteria. The strength, wind direction, and altitude of an SBJ case are defined by the time-averaged, case-mean value of V_{maxprof}.

A total of 65 SBJ cases were tagged at SHS during the six cool seasons. Of those, we chose approximately the strongest tercile of cases (i.e., the 20 strongest) with

TABLE 2. Chronological list and case-mean attributes of the 20 strongest SBJ cases at the SHS wind profiler (out of a total of 65 SBJ cases) for the cool-season window in water years 2006–11. The second-to-last column indicates the presence (Yes) or absence (No) of an AR impacting California in either the morning or afternoon composite SSM/I IWV satellite imagery within the date range of each SBJ case. The last column shows the time offset of the WRF-RD SBJs relative to the observed SBJs at SHS for the 13 most recent of the 20 cases. The 20-case averages (avg) and standard deviations σ of the case-mean attributes are given at the bottom.

Case	SBJ core time and date	SBJ start time and date	SBJ case duration (h)	SBJ $V_{maxprof}$ mean altitude (m MSL)	SBJ $V_{maxprof}$ mean magnitude ($m\,s^{-1}$)	SBJ $V_{maxprof}$ mean direction (°)	AR in CA, based on SSM/I	SBJ core offset in WRF (h)
1	1330 UTC 31 Dec 2005	1400 UTC 30 Dec 2005	26	494	22.4	164.7	Yes	
2	1030 UTC 27 Feb 2006	1900 UTC 26 Feb 2006	28	1051	26.7	162.5	Yes	
3	0830 UTC 6 Mar 2006	1000 UTC 5 Mar 2006	27	968	20.4	162.4	Yes	
4	1330 UTC 3 Apr 2006	2100 UTC 2 Apr 2006	21	1106	20.9	162.5	Yes	
5	2030 UTC 11 Apr 2006	0900 UTC 11 Apr 2006	31	1639	20.3	165.8	Yes	
6	0630 UTC 26 Jan 2008	2000 UTC 25 Jan 2008	18	1760	28.8	157.8	Yes	
7	1730 UTC 24 Feb 2008	1300 UTC 24 Feb 2008	10	564	21.8	162.9	Yes	
8	1630 UTC 19 Jan 2010	0300 UTC 19 Jan 2010	40	869	24.5	169.1	Yes	0.5
9	0530 UTC 5 Feb 2010	0000 UTC 5 Feb 2010	19	798	21.7	157.6	Yes	1.5
10	0530 UTC 24 Feb 2010	1900 UTC 23 Feb 2010	23	834	21.2	157.2	Yes	8.5
11	0230 UTC 21 Nov 2010	2100 UTC 20 Nov 2010	9	792	21.0	171.2	Yes	0.5
12	1030 UTC 6 Dec 2010	0700 UTC 6 Dec 2010	10	631	21.6	168.4	Yes	−1.5
13	0830 UTC 22 Dec 2010	2000 UTC 21 Dec 2010	17	1358	20.7	161.1	Yes	0.5
14	0530 UTC 29 Dec 2010	2300 UTC 28 Dec 2010	12	482	21.9	166.8	Yes	0.5
15	1830 UTC 14 Feb 2011	1000 UTC 14 Feb 2011	20	1158	21.7	165.2	Yes	3.5
16	0830 UTC 16 Feb 2011	0300 UTC 16 Feb 2011	8	1183	22.5	175.9	Yes	1.5
17	1430 UTC 25 Feb 2011	0300 UTC 25 Feb 2011	15	621	22.4	171.0	Yes	−2.5
18	1330 UTC 2 Mar 2011	0700 UTC 2 Mar 2011	17	851	24.6	163.1	Yes	0.5
19	1730 UTC 18 Mar 2011	1200 UTC 18 Mar 2011	9	1434	21.5	173.6	No	3.5
20	0730 UTC 20 Mar 2011	1100 UTC 19 Mar 2011	34	806	26.2	160.6	Yes	6.5
	20-case strongest	(Avg/σ)	19.7/9.2	970/85	22.6/6.0	165/5.7		

uninterrupted hourly wind profiles (Table 2, which includes the 20-case averages and standard deviations) in order to focus on the hydrometeorologically important cases. Neiman et al. (2010) showed that the strongest cases measured by the nearby CCO wind profiler during a 7-yr period produced the heaviest precipitation. All but one of the 20 strongest SBJs at both SHS and CCO occurred during the landfall of an AR in California (Table 2), as determined by Special Sensor Microwave Imager (SSM/I) IWV satellite measurements (Hollinger et al. 1990).[1] In contrast, for the 20 weakest SBJ cases at

[1] If the SSM/I imagery showed a long (>2000 km), narrow (<1000 km) plume of enhanced IWV (>2 cm) intersecting the California coast during the morning or afternoon on a given day, then that day was tagged an AR day. The same IWV threshold was employed in Ralph et al. (2004) and Neiman et al. (2008a,b) to define an AR.

SHS (CCO), only 9 (11) AR landfalls were observed. For the present study, the composite orientation of the ARs making landfall for the 20 strongest SBJs is from 220° to 40° (see section 5, Fig. 9d).

To assess the temporal–vertical evolution of the 20 strongest SBJ cases at SHS, composite 24-h duration time–height analyses were generated, where the hourly profile with the largest V_{maxprof} for each case (i.e., the SBJ core, or V_{max}) was designated as the center time (i.e., $t = 0$ h), and the temporal endpoints were taken as ±12 h of the SBJ core. Given that SBJ cases ranged in duration from 8 to 40 h (Table 2), the endpoints did not necessarily align with the start and/or end of SBJ conditions. However, this approach will provide a composite depiction during the core SBJ period. The 20 cases were averaged, yielding a composite of 25 hourly profiles, from which time–height analyses of Sierra-parallel (from 160°) and AR-parallel (from 220°) isotachs were constructed (Figs. 2a,b). In these analyses, shallow terrain-trapped southerly flow increases in magnitude with time early in the compositing period, culminating in a shallow SBJ core of 25.7 m s^{-1} from 161° (i.e., nearly perfectly aligned with the Sierra) at 681 m MSL. Above the developing SBJ, strengthening southwesterly flow descends in response to approaching AR conditions, with AR-parallel isotachs eventually exceeding ~20 m s^{-1} (similar to that observed in a case study by Kingsmill et al. 2013). Following the SBJ core, the flow veers from southerly to southwesterly between ~0.5 and 2.0 km MSL and the AR-parallel isotachs weaken, thus marking the passage of a cold front aloft. Below ~0.5 km MSL, terrain-blocked southerly flow persists but weakens.

For a regionwide observational composite depiction of SBJ evolution across California's northern CV during the strongest SBJ cases at SHS, we present concurrent wind profiler composite time–height analyses at CFC, CCO, CCR, and BBY. However, the five sites collected data simultaneously only during the cool seasons of 2009/10 and 2010/11. Thirteen of the 20 strongest SBJ cases at SHS occurred during those two cool seasons (Table 2), and composite time–height analyses based on the subset of cases are shown in Figs. 2c and 2d. The 13-case composite analyses are nearly identical to, and, hence, representative of, their 20-case counterparts in Figs. 2a and 2b. Also, composite profiles and standard deviations of wind speed and direction for the SBJ core hour (Fig. 3) are comparable. Plan-view precipitation analyses were constructed using NOAA/NCEP's Stage IV gridded dataset, both for the 20-case and 13-case SBJ composites (Fig. 4). Those 6-h-resolution gridded analyses that fell within, or no more than 2 h outside of, each SBJ case observed at SHS were included in the compositing. The precipitation analyses are nearly identical, thus providing additional evidence that the 13-case SBJ composite accurately represents the larger 20-case composite. The wind profilers (surface stations) in the present study are located in regions of light (heavy) composite precipitation.

4. Observed composite characteristics of the SBJ and AR

Given the similarities between the 20-case and 13-case composite wind profiler analyses of SBJ cases at SHS (Fig. 2) and the companion plan-view precipitation analyses (Fig. 4), this section will focus on the 13-case composites when simultaneous wind profiler data are also available at CFC, CCO, CCR, and BBY. Concurrent surface and GPS data are also analyzed.

a. Wind profiler network

Figure 5 shows simultaneous 13-case composite time–height analyses of Sierra-parallel isotachs from the four wind profilers across the northern CV region. The SBJ at SHS over the CV (Fig. 5a) has a core value of 26.9 m s^{-1}, is aligned with the Sierra (i.e., directed from 162°), resides at 704 m MSL, and, by definition, occurs at hour = 0. In contrast, the adjacent wind profiler at CFC in the Sierra foothills (Fig. 5b) documents a weaker SBJ core (22.3 m s^{-1}) directed from the south (178°) at a much higher altitude (1663 m MSL) and at a slightly later time ($t = 0.5$ h). The difference in altitude and wind direction of the SBJ core across the Sierra's windward slope confirms its terrain-following character, which was also reported in case studies (e.g., Parish 1982; Rauber 1992; Kingsmill et al. 2013) and in the composite study by Neiman et al. (2010) that utilized multiyear but nonsimultaneous observations from the CCO and Grass Valley wind profilers (located in the CV and Sierra foothills, respectively) farther north.

The composite SBJ altitude at CCO (Fig. 5c; 1232 m MSL) matches the average of the 20 strongest cases in Neiman et al. (2010) (1241 m MSL), even though the two studies do not have overlapping cases. The SBJ core at CCO is higher than at SHS, consistent with the case study results of Kingsmill et al. (2013) showing a poleward increase in altitude of the SBJ over the northern CV. They hypothesized that an observed northward increase in precipitation along the northern Sierra (similar to the composite observations in Fig. 4) yielded enhanced diabatic cooling (e.g., melting) toward the north, allowing larger amounts of cool air to be injected into the northern CV through low-level downslope flow in river valleys along the west slope of the Sierra (e.g., Steiner et al. 2003). This process would foster a poleward deepening of the stable air mass in the CV. The SBJ at

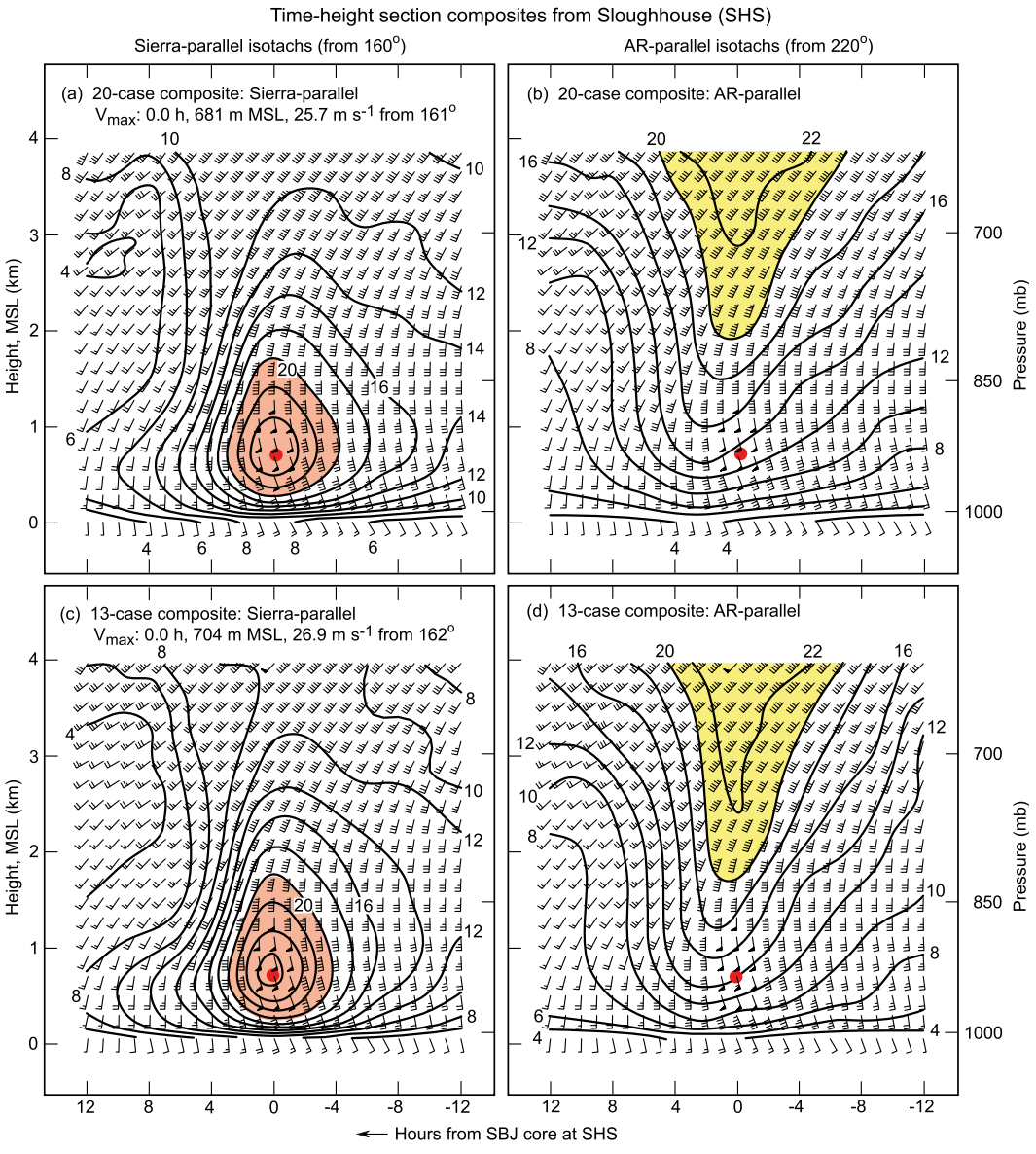

FIG. 2. Composite 24-h duration time–height sections of hourly averaged wind profiles (flags, 25 m s^{-1}; barbs, 5 m s^{-1}; half barbs, 2.5 m s^{-1}) and isotach components (m s^{-1}) during SBJs observed at SHS: (a) 20-case Sierra parallel (directed from 160°), (b) 20-case AR parallel (directed from 220°), (c) 13-case Sierra parallel, and (d) 13-case AR parallel. Red and yellow shading correspond to >20 m s^{-1} Sierra- and AR-parallel flow, respectively. Time = 0 h corresponds to the time of each SBJ core (i.e., V_{max}) observed at SHS. The red dot in each panel marks the time and altitude of V_{max}, the attributes of which are also given. Time increases from right to left to portray the advection of synoptic features from west to east.

CCO is weaker (23.5 m s^{-1}) than at SHS and more closely aligned with the Sierra (168°) than in the foothills above CFC. The SBJ core at CCO occurs 2 h earlier than at SHS and reflects a general equatorward movement of cold fronts and associated prefrontal dynamics that help sustain the SBJs (Neiman et al. 2010; Kingsmill et al. 2013).

A composite time–height analysis from CCR (Fig. 5d), located west of the CV in the coastal mountain gap of San Francisco Bay (i.e., the SFB gap), also shows a low-level maximum in the Sierra-parallel component (17.9 m s^{-1} at 1355 m MSL). However, the flow in this maximum is from 203° rather than oriented nearly parallel to the Sierra and therefore represents the transient pre-cold-frontal low-level jet rather than the terrain-locked SBJ captured by the three more eastern wind profilers. The low-level jet at CCR occurs 2.5 h after the same jet is observed along the

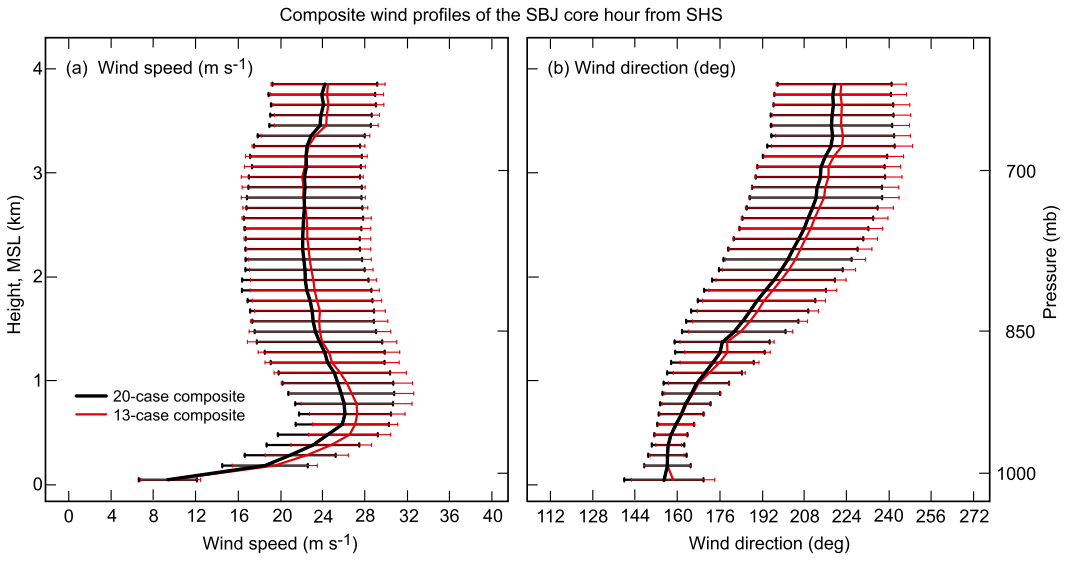

FIG. 3. Composite profiles with standard deviation bars (black and red are the 20- and 13-case composites, respectively) during the SBJ core hour (i.e., time = 0 h in Fig. 2) observed at SHS: (a) wind speed ($m\,s^{-1}$) and (b) wind direction (°).

coast at BBY (not shown) and 2 h prior to the SBJ core at SHS, thus pointing to the connection between landfalling cold fronts and SBJ evolution. Kingsmill et al. (2013) used a scanning radar to highlight the fact that the western edge of SBJ flow in their case study was positioned east of CCR, consistent with our composite observations.

The composite AR-parallel component of the flow measured by the wind profilers is shown in Fig. 6. These time–height analyses share the following attributes:

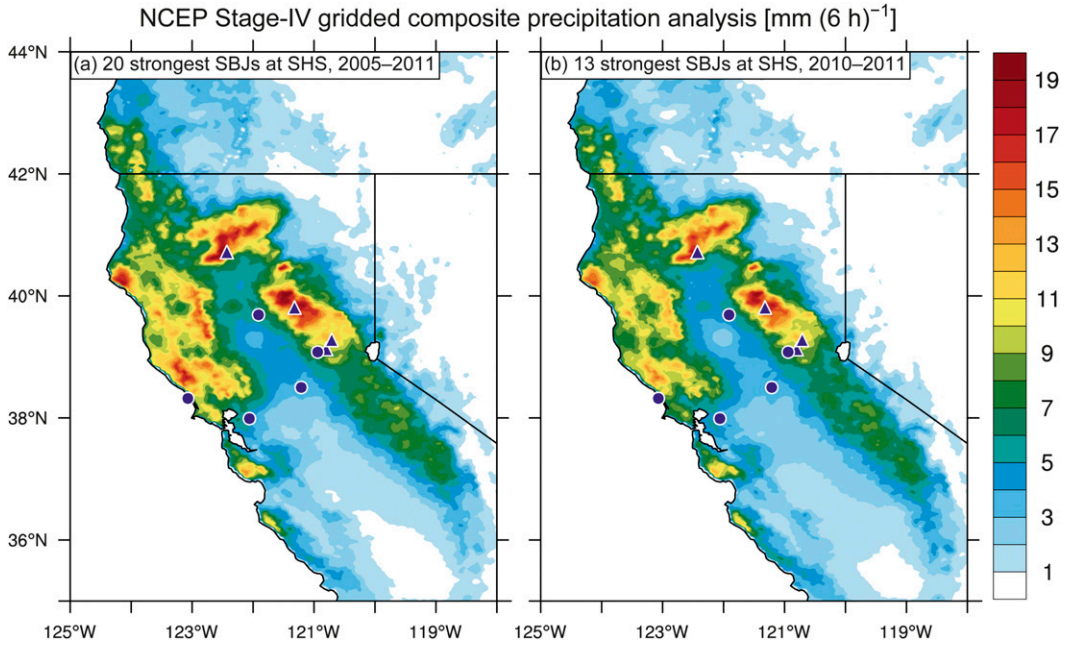

FIG. 4. Composite precipitation rate [mm $(6\,h)^{-1}$] from NCEP Stage IV gridded precipitation dataset for the following SBJ cases observed at SHS: (a) the 20 strongest during the cool seasons of 2005/06 through 2010/11 and (b) the remaining 13 strongest during the cool seasons of 2009/10 through 2010/11. The circles and triangles are as in Fig. 1.

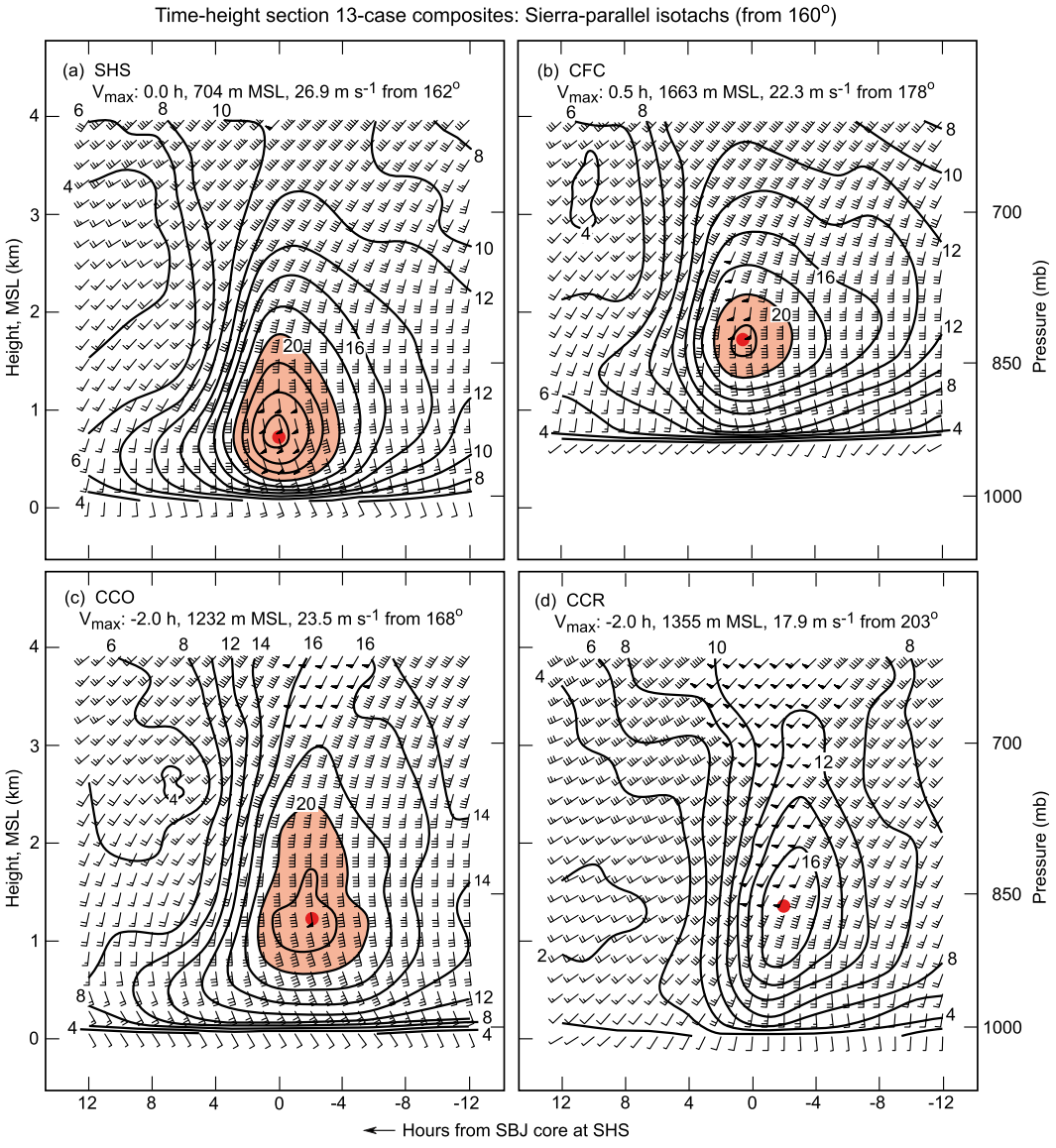

FIG. 5. Composite, 13-case, 24-h duration time–height sections of hourly averaged wind profiles (as in Fig. 2) and Sierra-parallel isotachs ($m\,s^{-1}$; directed from 160°; $>20\,m\,s^{-1}$ red shaded) at (a) SHS, (b) CFC, (c) CCO, and (d) CCR. Time = 0 h corresponds to the time of each SBJ core (i.e., V_{max}) observed at SHS. The red dot in each panel marks the time and altitude of the site-specific V_{max}, the attributes of which are also given. Time increases from right to left, as in Fig. 2.

i) the temporal descent and intensification of southwesterly flow during the approach of pre-cold-frontal AR conditions above the strengthening Sierra-parallel flow, ii) the temporal alignment of the strongest AR flow aloft with the shallow Sierra-parallel maximum, and iii) a well-defined, deep-layer temporal decrease in the magnitude of southwesterly flow marking the passage of a cold front over the decaying Sierra-parallel maximum. At the three sites closest to the Sierra (SHS, CFC, CCO), shallow (<1 km MSL) SBJ flow persisted beneath cold-frontal conditions aloft in response to remnant blocking. The profiler located farthest from the Sierra (CCR) recorded stronger southwesterly flow in the AR that descended closer to the surface than at the three other sites, a consequence of less orographic diversion of flow into the Sierra-parallel component.

b. *Surface and GPS networks*

Composite time series of surface parameters and IWV (Fig. 7), in tandem with the time–height sections above, provide additional insight into the meteorology associated with the SBJs and landfalling ARs. Surface temperatures

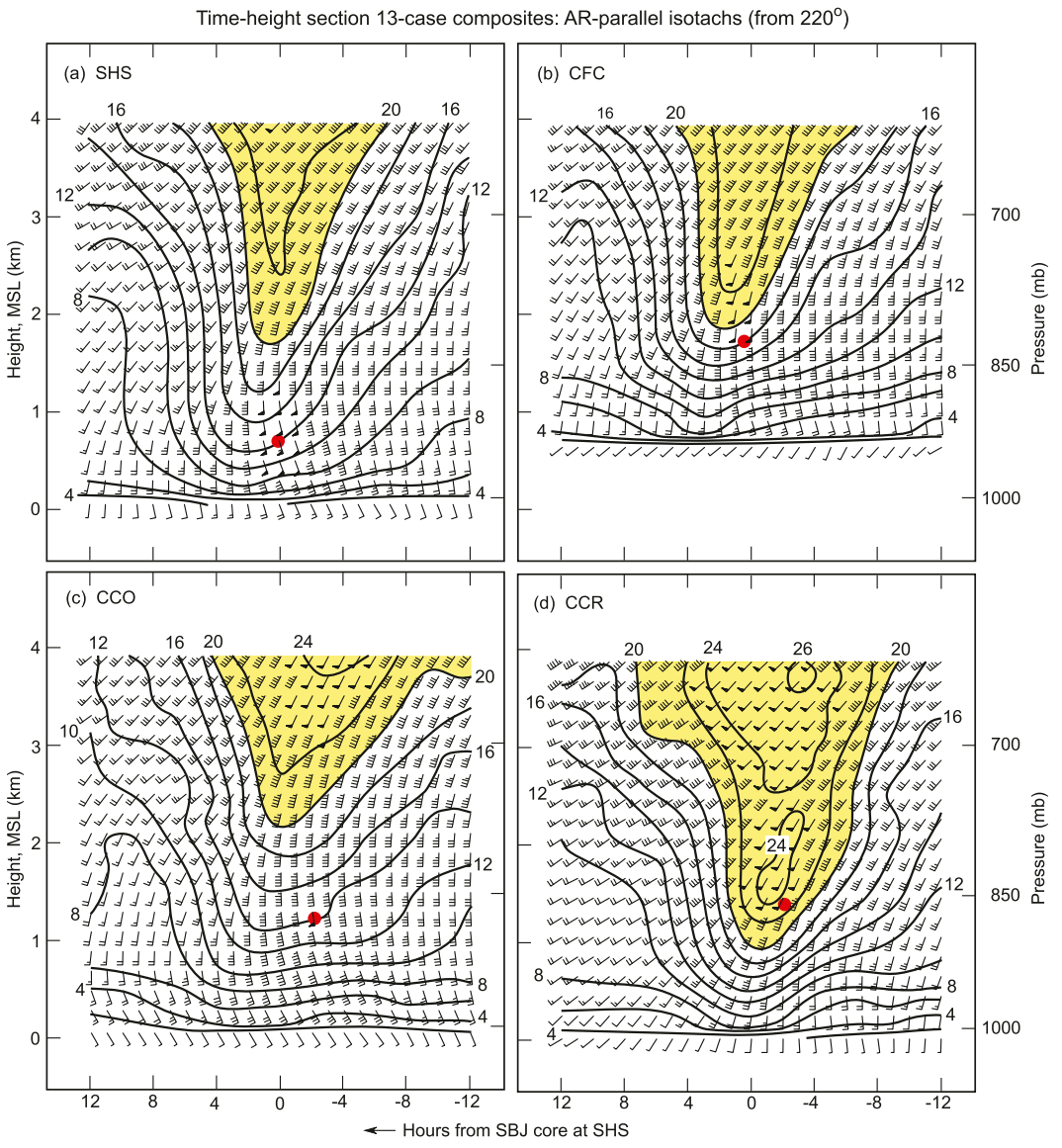

FIG. 6. As in Fig. 5, but for AR-parallel isotachs (directed from 220°; >20 m s^{-1} yellow shaded).

vary little during the 24-h period (Fig. 7a), but they decrease with increasing altitude and increase with decreasing distance to the coast (i.e., increasing distance from the SBJ). The station pressure traces (Fig. 7b) show a trough near the strongest SBJ flow, thus suggesting a dynamical connection between the approach of a cold front aloft (greater than ~1.5 km MSL) and the shallow SBJ. Following the trough axis passage, conditions become dynamically less favorable for the SBJ and it weakens. IWV traces at the four profilers (Fig. 7c) reveal tropospheric moistening in the pre-cold-frontal AR airstream during the 12-h period leading up to the SBJ core, with a broad peak exceeding the 2-cm threshold for AR conditions (e.g., Ralph et al. 2004) at the three sites near sea level. Thereafter, a decrease in IWV marks tropospheric drying in the cold front following the passage of the pressure trough. Collocated surface observations of water vapor specific humidity (q; Fig. 7d) at the three profilers located beneath the SBJ (SHS, CFC, CCO) reveal continued moistening for 5–6 h after their respective IWV maxima, thus suggesting that the terrain-blocked flow funnels shallow moisture poleward in the northern CV despite column-integrated drying in the cold front aloft. In contrast, the time lag at CCR between the IWV and surface q maxima is half that observed farther inland and consistent with the fact that the SFB gap is not dominated by SBJ flow.

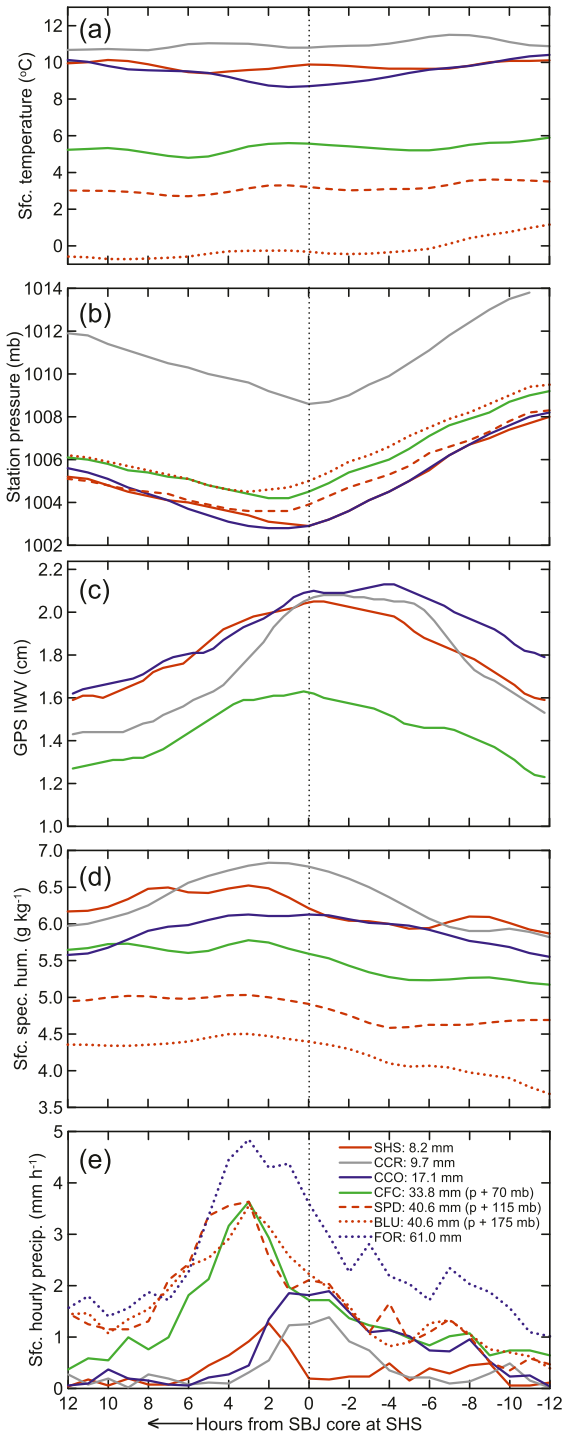

FIG. 7. Composite, 13-case, 24-h duration time series of surface and vertically integrated meteorological parameters: (a) surface temperature (°C), (b) station pressure (mb), (c) vertically integrated water vapor (cm), (d) surface water vapor specific humidity (g kg^{-1}), and (e) hourly precipitation (mm h^{-1}). Panel (e) contains a legend showing the site names, total composite precipitation accumulation at each site, and station pressure offsets for the high-elevation sites. Time = 0 h (thin vertical dotted lines) corresponds to the time of each SBJ core (i.e., V_{max}) observed at SHS.

Time series of composite hourly precipitation at the four profilers and three additional surface sites (Fig. 7e) can be separated into two geographic zones: the valley (SHS, CCO, CCR) where daily precipitation ranged from ~8 to 17 mm, and the foothills (CFC, SPD, BLU, FOR), where much larger daily totals of ~34–61 mm were observed. The valley sites show a 1–2 mm h^{-1} maximum occurring ≤2 h after the SBJ core during the initial phase of cold-frontal passage aloft, likely in response to frontal dynamics. In contrast, the foothills sites exhibit a much larger 3.5–4.8 mm h^{-1} maximum occurring 2–5 h after the SBJ core when southerly flow is shifting to southwesterly in the layer between 1 and 2 km MSL. Precipitation persists in the foothills thereafter. The fact that the wind shift yields flow directed more orthogonal to the Sierra crest, in conjunction with inferred static destabilization based on moistening at low levels with drying aloft, suggests an orographic forcing component to this maximum, as now will be demonstrated.

c. *Orographic precipitation diagnostics*

To quantify the role of orographic forcing on the generation of precipitation, we employ the methodology in Neiman et al. (2002, 2009) to calculate vertical profiles of linear correlation coefficient between composite time series of hourly upslope IWV flux versus precipitation rate. The upslope IWV flux is the product of the terrain-normal component of the flow measured hourly by a wind profiler and the hourly IWV measured by a GPS receiver at the same site. The upslope flow is calculated in 500-m layers centered on each profiler range gate. Because water vapor is typically concentrated in the lower troposphere, the IWV flux is a first-order estimate of the low-level vapor flux. Three observing couplets, each composed of a wind profiler in the CV and a downwind precipitation gauge in the foothills, are used: 1) SHS-BLU (97-km distance, oriented at 207°–27°), 2) CCO-FOR (52-km distance, oriented at 255°–75°), and 3) CCO-STD (122-km distance, oriented at 159°–339°). The first two couplets assess the orographic forcing in the Sierra foothills where the upslope component of the flow, from 250°, is perpendicular to the Sierra crest (i.e., nearly parallel to the AR). The third couplet evaluates the orographic forcing at the base of the Shasta–Trinity Alps at the north end of the CV, where the upslope component, from 160°, is aligned orthogonal to those mountains and along the SBJ.

The correlation profiles (Fig. 8a) show distinctive characteristics related to the orography. The couplets in the Sierra foothills (SHS-BLU and CCO-FOR) contain a correlation maximum (hereafter, the orographic controlling layer) at ~1.5 km MSL (r = 0.962 and 0.958, respectively) associated with moist southwesterly flow.

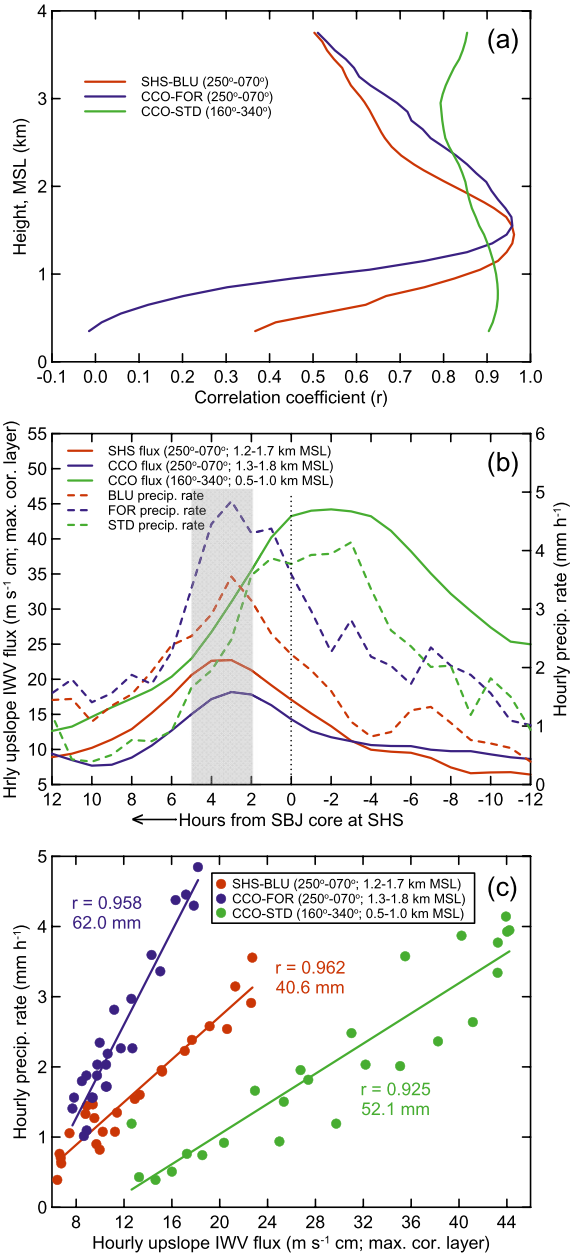

FIG. 8. Composite, 13-case, 24-h duration orographic precipitation analysis from the wind profiler–precipitation gauge couplets at SHS-BLU (red curves; upslope direction from 250°), CCO-FOR (blue curves; upslope direction from 250°), and CCO-STD (green curves; upslope direction from 160°). (a) Vertical profiles of linear correlation coefficient, based on hourly averaged profiles of upslope IWV flux vs hourly precipitation rate. (b) Time series of upslope IWV flux (solid lines) in the layer of maximum correlation coefficient (1.2–1.7 km MSL at SHS-BLU, 1.3–1.8 km MSL at CCO-FOR, 0.5–1.0 km MSL at CCO-STD) and hourly precipitation rate (dashed lines). Time = 0 h (thin vertical dotted line) corresponds to the time of each SBJ core (i.e., V_{max}) observed at SHS. The shaded rectangle denotes the 3-h cold-frontal period based on the WRF-RD analysis in Fig. 11. (c) Scatterplot analyses and linear regression fits in the layer of maximum correlation coefficient. Numerical values of correlation coefficient r and composite accumulated precipitation are given.

The correlations decrease sharply downward toward the surface owing to the presence of the shallow SBJ, and they decrease upward into the middle troposphere above the Sierra crest. The altitude of the orographic controlling layer is ~50% higher than that observed along the California coast (i.e., ~1 km MSL; Neiman et al. 2002, 2009), partly because the mountains are higher and the blocked flow deeper than in the coastal zone. The controlling layer is ~100 m higher at CCO-FOR than at SHS-BLU, consistent with the fact that the SBJ core is higher at the more northern couplet (Figs. 5a,c). In contrast to the Sierra couplets, the CCO-STD couplet shows the importance of the SBJ in generating orographically enhanced precipitation at the windward base of the Shasta–Trinity Alps at the north end of the CV. A shallower, less prominent controlling layer at 0.75 km MSL (r = 0.925) resides within the SBJ at CCO and reflects the strong up-valley transport of water vapor toward Shasta–Trinity. The correlation remains large downward toward the surface in the SBJ flow. Aloft, the correlation does not decrease as much as its Sierra counterparts and it increases again above crest level (~3 km MSL); this behavior is likely linked to transient synoptic forcing aloft. The altitudes of the orographic controlling layer at the Sierra and Shasta–Trinity couplets are much lower than the level of 700 hPa (~3 km MSL) used for obtaining the direction of flow in the Rhea (1978) operational orographic precipitation model. However, the altitude at the Sierra couplet roughly matches that of the cool-season vapor flux maximum in Pandey et al. (1999), who used four decades of coarse temporal–vertical resolution (relative to the profiler) rawinsonde data from Oakland to quantify upstream impacts on orographic precipitation in the Sierra.

Composite time series of precipitation rate and upslope IWV flux at the controlling layer (Fig. 8b) reveal the close temporal relationship and orographic link between these two variables at each couplet. They also show that the strongest orographic forcing at the Sierra couplets occurs 2–5 h after the SBJ core when the wind shifts from southerly to southwesterly (i.e., the flow becomes more perpendicular to the axis of the Sierra; Figs. 5a,c) in the moist remnant AR airstream and in the dynamically forced cold-frontal zone. Roughly 56% of the precipitation at the Sierra gauges fell during SBJ conditions ($t \leq 2$ h), 21% during the cold-frontal passage ($5 \leq t \leq 2$ h), and 23% in post-cold-frontal conditions ($t \geq 5$ h). Unlike in the northern Sierra, the maximum orographic forcing at the north end of the CV coincides with the shallow SBJ core at CCO. This latter result supports the model-based study of Kim and Kang (2007) that used regional climate simulations to investigate the influence of the Sierra on the water cycle for a winter season. They

found that the SBJ transports significant moisture northward to the northern Sierra and CV terminus, resulting in increased rainfall there. Similarly, a 9-km-resolution WRF simulation of a flood-producing AR in California on 31 December 2005 (Smith et al. 2010) highlights the occurrence of a strong, shallow SBJ beneath an AR aloft, resulting in enhanced water vapor transport directed toward the north end of the CV where heavy precipitation fell. The orographic character of the precipitation in Northern California is highlighted further in Fig. 4, which shows the prominent AR-induced maximum along the windward slope of the northern Sierra and the SBJ-forced maximum in the Mt. Shasta–Trinity Alps region. A third set of maxima in the coast ranges northwest of SFB is likely forced by AR landfalls. This pattern resembles a coarser NARR composite for the 20 strongest SBJ cases observed at CCO (Neiman et al. 2010).

The data in Fig. 8b are also shown in scatterplot format (Fig. 8c) to further highlight the robust linkage between these time series when 41–62 mm of precipitation fell in 24 h at the foothills sites. The linear regression slope is greater at CCO-FOR than at SHS-BLU or CCO-STD and is explainable, in part, by the case study results of Reeves et al. (2008). They found that an SBJ may have enhanced precipitation along a prominent westward jog in the northern Sierra (i.e., the Feather River basin where FOR is located) because the SBJ encountered the terrain slope at a more perpendicular angle at that locale. The northernmost couplet possesses the least precipitation for a given IWV flux, partly because the orographic forcing resulting from the shallow, cold SBJ impacting Shasta–Trinity likely has greater static stability than the southwesterly airstream impacting the Sierra above the SBJ [e.g., see the WRF-RD static stability discussion in section 5b(1)]. Also, the difference in linear regression slope at the three couplets conforms qualitatively to the difference in local mean terrain slope along the upslope component of the flow at the three gauge sites (BLU, 2.9%; FOR, 3.5%; STD, 1.8%), in agreement with the implied upslope-induced ascent from the canonical linear upslope model (e.g., Smith 1979). Site placement of gauges relative to large-scale terrain features can also affect the linear regression slope.

5. Reanalysis composite perspective of the SBJ and AR

a. Synoptic context: The NARR

To gain synoptic-scale context during SBJ conditions observed at SHS, we generated NARR composite plan-view analyses (Fig. 9) using the two 3-h reanalysis times closest to the core time of each of the 13 SBJ cases at SHS, with the following constraint: the latter of the two NARR analyses for each case must be ≤30 min later than the corresponding SBJ core time so as to minimize the chance of cold-frontal conditions over SHS in the NARR.[2] An analysis at 300 hPa (Fig. 9a) shows a trough offshore of California and the exit region of a cyclonically curved jet—a favored region of ascent (Beebe and Bates 1955)—traversing the state from southwest to northeast. At 500 hPa (Fig. 9b), the trough is sharper, and cyclonic vorticity advection (CVA) indicative of quasigeostrophic ascent (given the assumption CVA increases with height) is making landfall over Northern California. A low-level analysis at 900 hPa (Fig. 9c) depicts a closed cyclone offshore of Vancouver Island and southwesterly flow impacting California immediately downstream of a sharp trough axis, which marks the leading edge of cold advection associated with an advancing polar cold front.

A diagnostic analysis of vertically integrated horizontal water vapor transport (IVT) between the surface and 300 hPa (Fig. 9d; methodology in Neiman et al. 2008b) contains a narrow plume of enhanced vapor fluxes (as large as $350\,\mathrm{kg\,s^{-1}\,m^{-1}}$) impacting California from the southwest (i.e., from ~220°, the AR-parallel orientation) that mirrors landfalling ARs (e.g., Neiman et al. 2008a,b). The enhanced IVT extends downwind from the SFB gap into the CV, then northward up valley in the terrain-trapped flow, similar to that captured by the NARR during strong SBJs at CCO (Neiman et al. 2010) and modeled by Smith et al. (2010) during a high-impact AR event. In addition, a thin band of enhanced IVT is situated along the Sierra crest and likely arises because of accelerated cross-mountain flow aloft.

In contrast to the synoptic composite analyses for the 20 strongest SBJ cases at SHS, the composites for the 20 weakest cases (not shown) exhibit a weaker, lower-amplitude, northward-displaced trough, and correspondingly weaker winds, vorticity, and IVT. In short, strong SBJs are tied, on average, to high-amplitude troughs impacting California and strong vapor fluxes intersecting the state from the southwest, whereas weak SBJs occur with low-amplitude troughs making landfall farther north and weaker zonally oriented vapor flux plumes. These dichotomous synoptic characteristics for strong versus weak SBJs mirror the results of the study by Neiman et al. (2010) that used the wind profiler observations at CCO.

[2] Based on the 20- and 13-case SBJ composite analyses at SHS (Figs. 2a,c), the SBJ typically strengthens gradually but terminates abruptly with a cold-frontal passage.

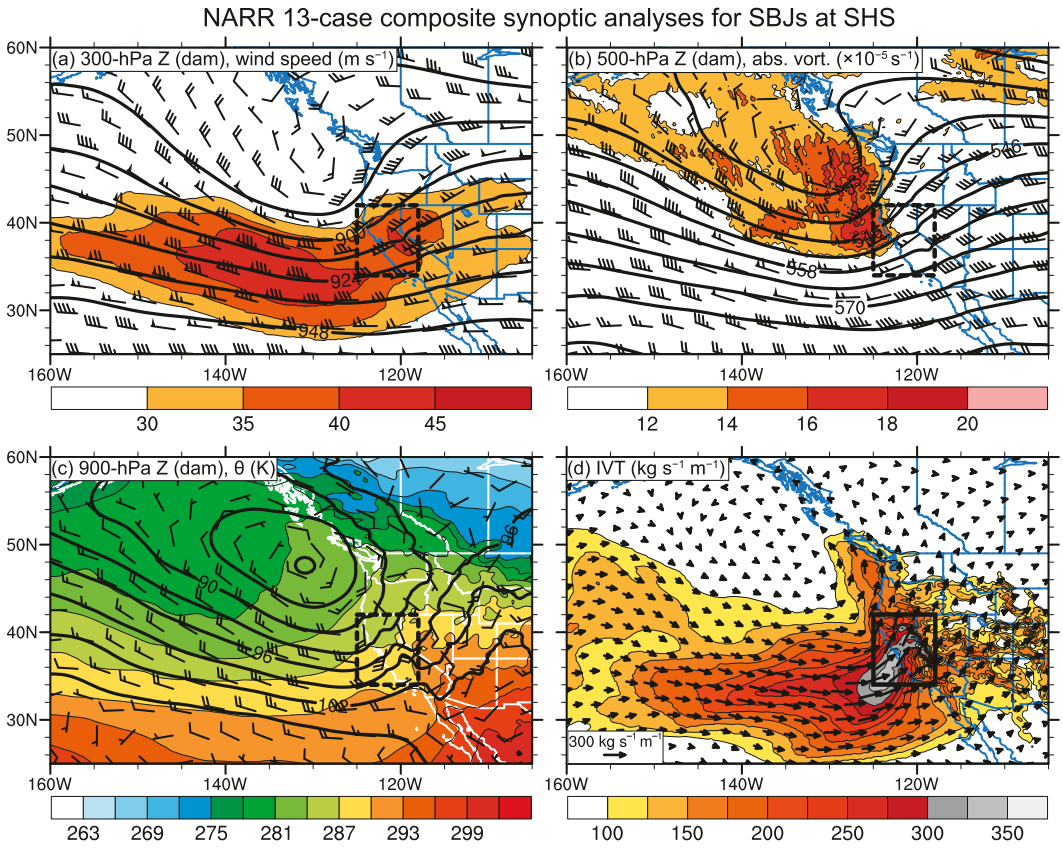

FIG. 9. Composite, 13-case, synoptic plan-view analyses derived from the NARR 3-h gridded dataset for SBJ core conditions observed by the SHS wind profiler: (a) 300-hPa geopotential height contours (Z; dam), isotachs ($m\,s^{-1}$; color fill), and wind velocities; (b) 500-hPa Z (dam), absolute vorticity ($\times 10^{-5}\,s^{-1}$; color fill), and wind velocities; (c) 900-hPa Z (dam), θ (K; color fill), and wind velocities; and (d) 1000–300-hPa IVT [$kg\,s^{-1}\,m^{-1}$; color fill with vectors (inset magnitude scale shown)]. Wind velocities in (a),(b), and (c) are described in Fig. 2. The inset black box in each panel shows the plan-view domain of the WRF-RD analyses in Fig. 10.

b. *Mesoscale details: The WRF-RD*

The inset black box in each panel of Fig. 9 marks the composite plan-view analysis domain of the high-resolution WRF-RD (Fig. 10); these analyses incorporate the time of the simulated SBJ core at the grid point closest to SHS. Each of the 13 SBJ cases observed by the SHS wind profiler has an SBJ counterpart in the hourly resolution WRF-RD,[3] although the timing of the 13 SBJ cores in the WRF-RD ranges from −2.5 to +8.5 h relative to the observations (see Table 2). For creating the WRF-RD composites, the time of the simulated SBJ core for each case was designated as the center time and the temporal endpoints were taken at ±12 h of the simulated SBJ core, analogous to the methodology employed for the observations. Figure 10 shows the locations of the grid points closest to the four interior wind profilers.

1) TIME–HEIGHT ANALYSES

Before the WRF-RD plan-view analyses are discussed, we assess the realism of this gridded dataset by validating against the wind profiler observations. Composite time–height sections of WRF-RD data for the grid point closest to SHS are presented in Fig. 11.[4] The WRF-RD analyses of Sierra- and AR-parallel isotachs (Fig. 11a) resemble their observed counterparts at SHS (Figs. 5a, 6a), although the magnitudes of the simulated wind components (including that of V_{max}) are slightly weaker. The altitude at which V_{max} occurs and the wind direction in this core are nearly identical in the WRF-RD and observations (Table 3). At the four other profiler

[3] The WRF-RD provides instantaneous data at the top of each hour, whereas the wind profiler observations are hourly averages valid at the bottom of each hour.

[4] The WRF-RD hourly wind profiles here are interpolated to the altitudes of the wind profiler range gates at SHS.

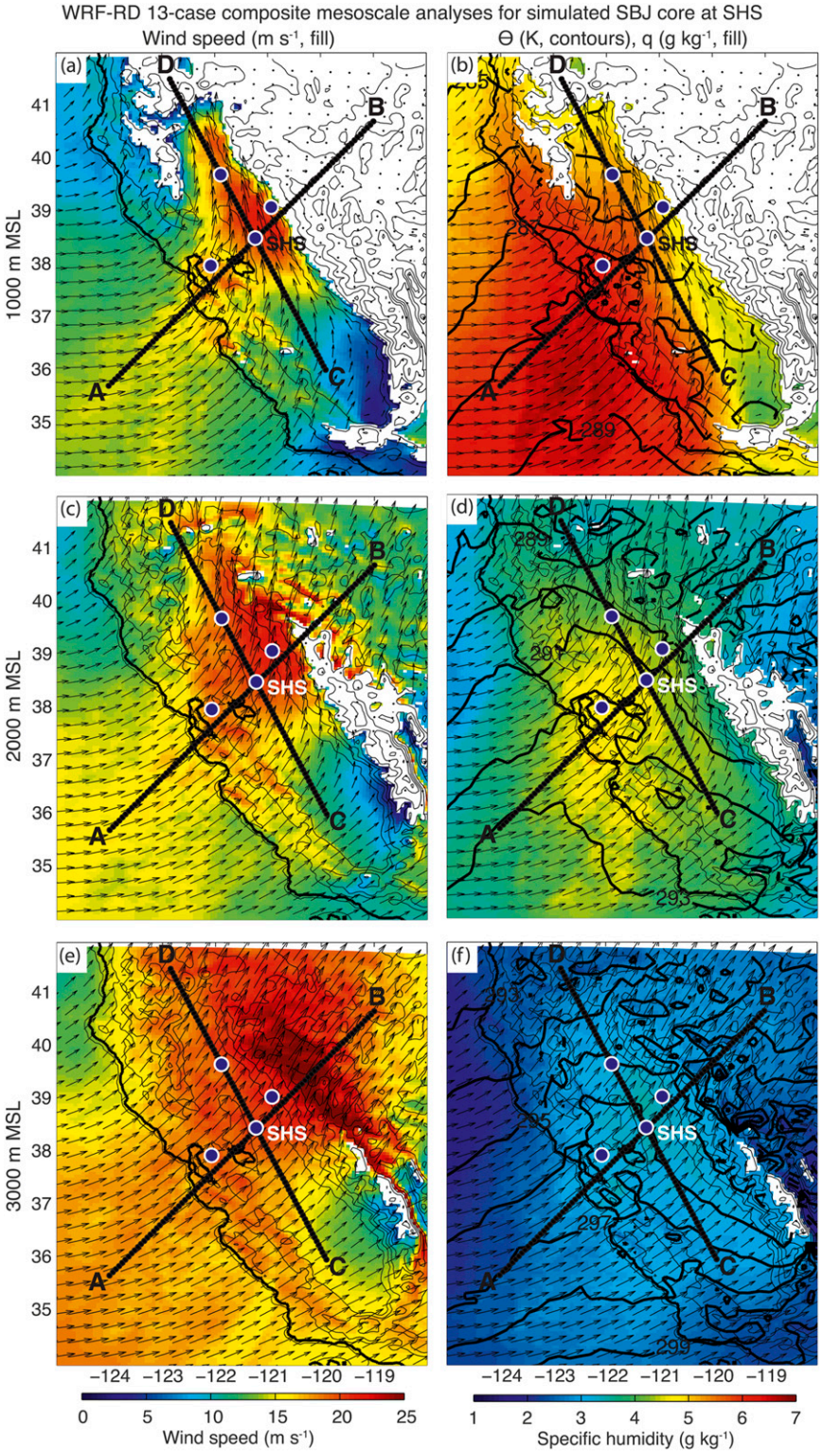

FIG. 10. Composite, 13-case, mesoscale (left) kinematic and (right) thermodynamic plan-view analyses derived from the WRF-RD gridded dataset for the hour of the simulated SBJ core (i.e., V_{max}) at the grid point closest to SHS. (a),(b) The 1000-m MSL wind speed ($m\,s^{-1}$; color fill) and θ (K; thick black contours, 1-K interval) with q ($g\,kg^{-1}$; color fill). Wind vectors portray wind speed (see also color fill in left column) and direction. The thin black contours represent model-resolution terrain (every 800 m starting at 100 m MSL). The thick black line shows the actual coastline. The heavy black lines A–B and C–D are projections for the cross sections in Fig. 12. The blue circles mark the horizontal grid points closest to the four interior wind profiler sites shown in Fig. 1 (SHS is labeled). (c),(d) As in (a),(b), but for 2000 m MSL. (e),(f) As in (a),(b), but for 3000 m MSL.

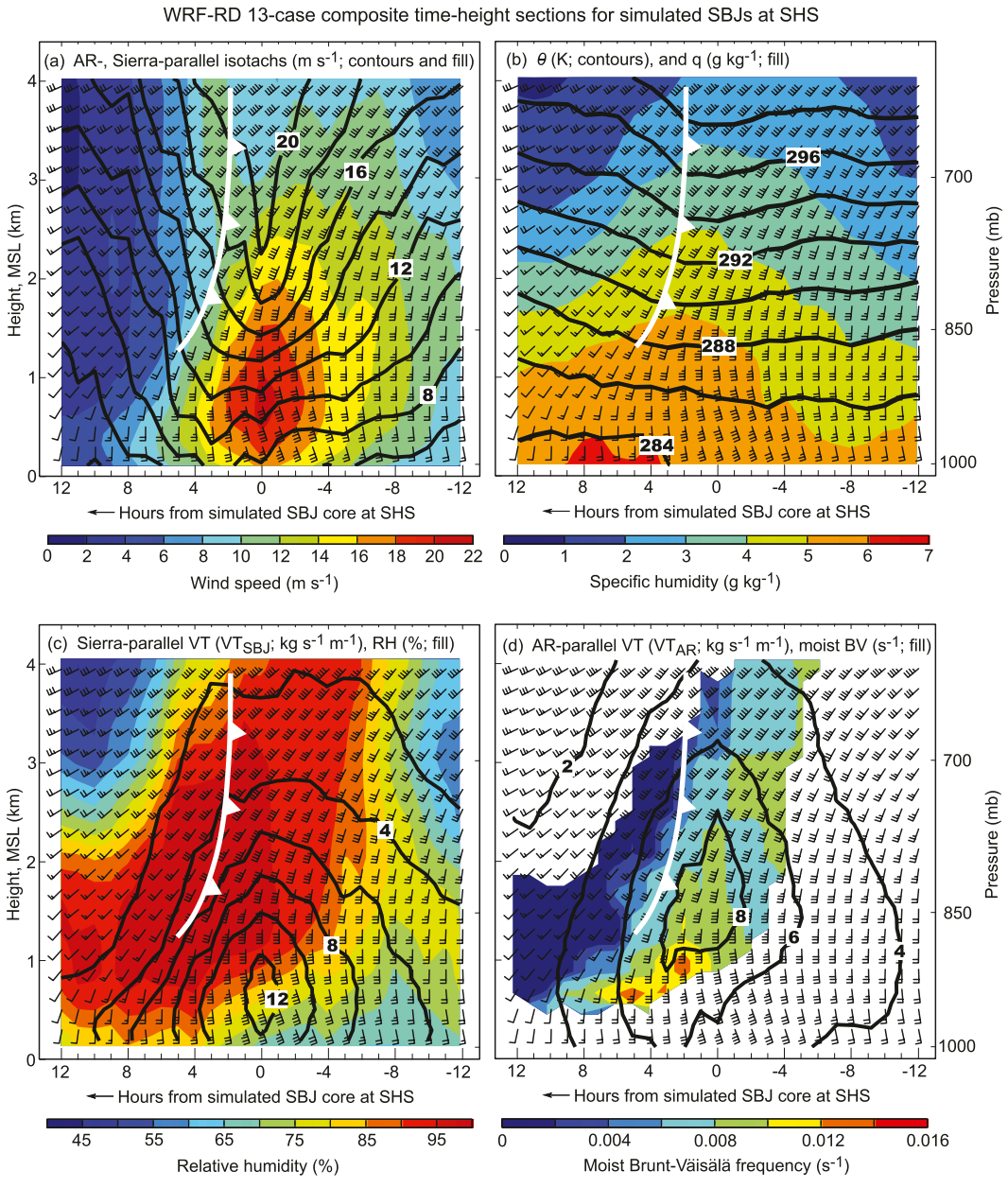

FIG. 11. Composite, 13-case, 24-h duration time–height sections of hourly wind profiles derived from the WRF-RD gridded dataset for simulated SBJs at the horizontal grid point closest to SHS: (a) AR-parallel isotachs ($m\,s^{-1}$, directed from 220°; black contours) and Sierra-parallel isotachs ($m\,s^{-1}$, directed from 160°; color fill), (b) θ (K; black contours) and q ($g\,kg^{-1}$; color fill), (c) VT_{SBJ} ($kg\,s^{-1}\,m^{-1}$, directed from 160°; black contours) and RH (%; color fill), and (d) VT_{AR} ($kg\,s^{-1}\,m^{-1}$, directed from 220°; black contours) and N_m (s^{-1}; color fill) for relative humidities ≥90%. Time = 0 h corresponds to the time of each simulated SBJ core (i.e., V_{max}) at the horizontal grid point closest to SHS. Wind velocities are described in Fig. 2. The cold-frontal analysis is based on (b).

sites, V_{max} is modestly weaker in the WRF-RD, but again the companion wind directions closely match the observations (Table 3). The altitudes of the simulated V_{max} at the three sites within the SBJ (i.e., SHS, CFC, CCO) are similar to the observations, but they are ~300–600 m too low for the two sites closest to the coast. Nevertheless, the time of V_{max} at each site relative to its occurrence at SHS is essentially identical for the WRF-RD and observations (Table 3). Finally, the additive bias and root-mean-square error (RMSE) between the composite wind profiler and WRF-RD data for both the Sierra-parallel and -perpendicular components are small

TABLE 3. Comparison between the 13-case composite wind observations and the WRF-RD at each wind profiler site. Columns 2–5 show the bulk V_{max} characteristics of the observations (left-hand values in each column) and WRF-RD (right-hand values in each column). Column 6 shows the linear correlation coefficient between the wind profiler data and WRF-RD data for both the Sierra-parallel wind V_{160} and the Sierra-normal wind V_{250}. Columns 7 and 8 show the additive bias and RMSE between the wind profiler data and WRF-RD data for both V_{160} and V_{250}.

Site name	Time relative to V_{max} at SHS (h)	V_{max} magnitude ($m\,s^{-1}$)	V_{max} direction (°)	V_{max} altitude (m MSL)	Time–height correlation coefficient; V_{160}/U_{250}	Time–height bias; V_{160}/U_{250} ($m\,s^{-1}$)	Time–height RMSE; V_{160}/U_{250} ($m\,s^{-1}$)
SHS	0.0/0.0	26.9/20.7	162/162	704/702	0.971/0.982	−1.8/−0.5	2.3/1.2
CFC	0.5/0.5	22.3/20.4	178/175	1663/1453	0.935/0.988	−0.9/0.3	1.8/1.0
CCO	−2.0/−2.0	23.5/20.2	168/165	1232/1171	0.961/0.985	−2.4/0.1	2.8/1.1
CCR	−2.0/−2.0	17.9/15.1	203/192	1355/762	0.894/0.984	−2.4/−1.9	3.1/2.6
BBY	−4.5/−4.0	17.1/16.5	180/177	777/460	0.978/0.986	−1.3/0.1	1.7/0.8

($<|3\,m\,s^{-1}|$; Table 3), with WRF-RD biases mostly less than 0. Hence, we have confidence that, to first order, the WRF-RD provides a realistic spatiotemporal mesoscale depiction of the SBJ and related meteorology across Northern California. Additional confidence in the WRF-RD's ability to capture the SBJ is provided in Hughes et al. (2012) using 11 years of wind profiler observations at CCO as an observational anchor. They demonstrate that the WRF-RD reasonably represents the vertical structure of SBJs observed at CCO, as well as during shorter concurrent periods spanning 1–7 years at six additional wind profiler sites across the region. However, unlike in the present study, they did not validate the temporal evolution of SBJ cases.

The remaining WRF-RD composite time–height sections at SHS are presented in Figs. 11b–d. The analysis of potential temperature θ and q (Fig. 11b) shows a moist thermal ridge in the southwesterly flow of the landfalling AR situated above the shallow and cool SBJ, and the decay of the SBJ coinciding with a forward-sloping cold front and subsequent drying aloft. The cold front was previously diagnosed from GPS and profiler observations as a concurrent decrease in IWV and AR-parallel flow aloft coinciding with a low-level wind direction shift from strong southerly (in the SBJ) to weaker southwesterly (Figs. 6a, 7c). The front's forward slope likely arises because of its terrain-induced deceleration at low levels, a behavior documented previously over the windward Sierra (e.g., Reynolds and Kuciauskas 1988; Rauber 1992) as well as on the upwind side of mountain ranges worldwide (e.g., Bjerknes and Solberg 1921; Egger and Hoinka 1992; Schumacher et al. 1996; Doyle 1997; Braun et al. 1999a,b; Yu and Bond 2002; Neiman et al. 2004). Despite the post-cold-frontal drying and cooling aloft, the low levels continue to moisten in the remnant terrain-blocked low-level southerly flow (as was shown earlier with surface q data).

Composite time–height sections of WRF-RD water vapor transport (VT) directed parallel to the Sierra (from 160°, VT_{SBJ}) and parallel to the AR (from 220°, VT_{AR}) are presented in Figs. 11c and 11d. The VT_{SBJ} analysis, which depicts a transport maximum at ~0.7 km MSL and $t = 0$ h, quantifies the key role of the SBJ in transporting water vapor poleward toward the north end of the CV well below the ~3-km crest of the Sierra. The altitude of this core matches the height of the orographic controlling layer at the CCO-STD couplet (Fig. 8a). Superimposed relative humidity (RH) contours show nearly saturated conditions in the landfalling AR over the subsaturated SBJ core. Thereafter, the saturated air temporally descends to the altitude of the decaying SBJ core, while drying aloft marks the advancing cold-frontal zone. The companion VT_{AR} analysis depicts an elevated core of vapor transport centered at ~1.7 km MSL roughly 1 h after the SBJ core. The altitude of this core, which is directed nearly orthogonal to the long axis of the Sierra, roughly coincides with the height of the 1.5-km MSL orographic controlling layer over the northern Sierra foothills (Fig. 8a). An accompanying analysis of moist Brunt–Väisälä frequency N_m for RH $\geq$ 90% (i.e., a proxy for saturated conditions) shows the temporal descent of weakening moist static stability following the axis of maximum VT_{AR} (i.e., the back edge of the AR). The destabilization is occurring in response to cold-frontal cooling and drying aloft and low-level moistening in the decaying SBJ. The delayed onset of the VT_{AR} maximum and destabilization relative to the time of the SBJ core at $t = 0$ h likely contributes to the orographic precipitation maximum over the Sierra foothills several hours after the SBJ core (Fig. 8b). Also, N_m is weaker in the AR region aloft than in the shallow SBJ, consistent with greater orographic precipitation efficiency in the Sierra foothills than at the north end of the CV (Fig. 8c).

2) PLAN-VIEW ANALYSES

Composite WRF-RD plan-view wind velocity and θ/q analyses at the time of the simulated SBJ core at SHS are shown at three altitudes (Fig. 10). The analyses at 1 km MSL (Figs. 10a,b) depict enhanced terrain-parallel SBJ

flow in a cold pool over the northern CV. Dry air in the southern CV south of the SFB gap is advected northward into the SBJ and may account for the dry conditions preceding the SBJ core in the WRF-RD time–height analyses of q and RH (Figs. 11b,c) and in the observed time series of surface q (Fig. 7d). A ribbon of strong, moist southwesterly flow in the pre-cold-frontal airstream of the AR offshore accelerates through the gap, merges with the SBJ, and likely contributes to its deepening north of SHS (Fig. 5c) and to low-level moistening during and after the SBJ core at SHS (Figs. 11b,c). The AR airstream is responsible for the low-level south-southwesterly flow and concomitant maximum in the Sierra-parallel component observed at CCR (Fig. 5d), although that maximum was not part of the SBJ. Kingsmill et al. (2013) used a scanning radar to demonstrate that the western edge of the SBJ in their case study was positioned east of CCR, consistent with our composite results.

At 2 km MSL (Figs. 10c,d), the enhanced flow over the northern CV is more expansive but less channeled up valley than in the SBJ at 1 km. In addition, a warm axis resides over the CV rather than a cold pool. These characteristics reveal that this higher altitude is above the SBJ core. Offshore, the corridor of strong, moist southwesterly flow marks the AR near the leading edge of the polar cold front. The analyses at 3 km MSL (Figs. 10e,f) portray strong southwesterly flow across the domain and a warm, moist axis over the CV well above the shallow SBJ. The strongest flow is situated east of the Sierra crest because of leeside mountain-wave accelerations (e.g., Lilly and Zipser 1972; Smith 1979; Durran 1990). Polar baroclinicity in a drying air mass resides offshore.

3) CROSS-SECTIONAL ANALYSES

The vertical structure through the composite SBJ and AR is highlighted in AR-parallel and Sierra-parallel WRF-RD cross sections (Fig. 12; along lines A–B, C–D in Fig. 10). In the AR-parallel wind components cross section (Fig. 12a), the Sierra-parallel isotachs show a terrain-following SBJ whose largest values ($>20\,\mathrm{m\,s^{-1}}$) are a few hundred meters above the eastern CV and lower windward slope of the Sierra, confirming the representativeness of earlier case study results (e.g., Parish 1982; Kingsmill et al. 2013), the inference drawn in a recent SBJ climatology study (Neiman et al. 2010), and the profiler observations presented earlier in this study. The western edge of the SBJ lies between CCR and SHS. Concurrent AR-parallel isotachs portray the enhanced flow of the AR riding over the shallow SBJ and then accelerating down the lee slope of the Sierra in response to mountain-wave dynamics. The plane-parallel deceleration of AR-parallel flow up the Sierra's windward slope is suggestive of orographically forced convergence and/or a northward deflection of the flow. The companion cross section of water vapor transport (Fig. 12c) illustrates the shallow character of the poleward-directed VT_{SBJ} core below 1 km MSL over the Sierra's lower windward slope and the slantwise plume of enhanced VT_{AR} originating over the ocean and sloping over the SBJ to the Sierra crest. The AR-parallel cross section of θ and q (Fig. 12e) shows weakly sloped isentropes over the ocean, becoming more sloped over the CV where shallow cool air and the SBJ reside. Moist air over the ocean transitions to drier across the CV and up the Sierra's windward slope. Downwind of the Sierra crest, a plunging thermal ridge within dry air marks the leeside mountain wave.

The Sierra-parallel cross section over the CV provides additional insights on the structure of the SBJ and AR. Sierra-parallel isotachs (Fig. 12b) show a higher-altitude SBJ core at CCO than at SHS, consistent with the profiler observations and supportive of the Kingsmill et al. (2013) case study results. The lateral gradient of Sierra-parallel flow at the north end of the CV suggests orographic convergence. Farther south, the SBJ possesses a sharp boundary south of SHS, thus suggesting a connection between the incoming moist airstream through the SFB gap and the SBJ north of this gap. Above the SBJ, strong AR-parallel flow covers all but the south end of the CV. The Sierra-parallel water vapor transport (Fig. 12d) mirrors its wind component counterpart and shows shallow poleward transport of water vapor in the SBJ from SHS to the north end of the CV. Much weaker VT_{SBJ} encompasses the CV south of SHS, partly because the coastal mountains south of the SFB prevent the inland penetration of low-level moisture from the Pacific into the southern CV. The superimposed VT_{AR} contours show an elevated core of water vapor transport at ~1.7 km MSL directed toward the Sierra that resides downwind of the SFB gap over the SBJ near SHS. The lateral confinement of this core, which does not match its wind component counterpart (Fig. 12b), could arise because of orographic rainout along the coastal mountains north and south of the SFB gap (Fig. 4) in response to southwesterly AR flow impinging on those mountains. More generally, the vapor transport results in Figs. 12c and 12d support the case study findings of Kingsmill et al. (2013) that show strong northward transport of water vapor in an SBJ beneath northeastward-directed water vapor transport by an AR aloft. The thermodynamic cross section (Fig. 12f) highlights a poleward decrease in θ. Water vapor is deepest downwind of the SFB gap over SHS, and the low-level water vapor content is greater over the northern than southern CV because of the inland penetration of marine air through the gap and its subsequent northward diversion by the SBJ.

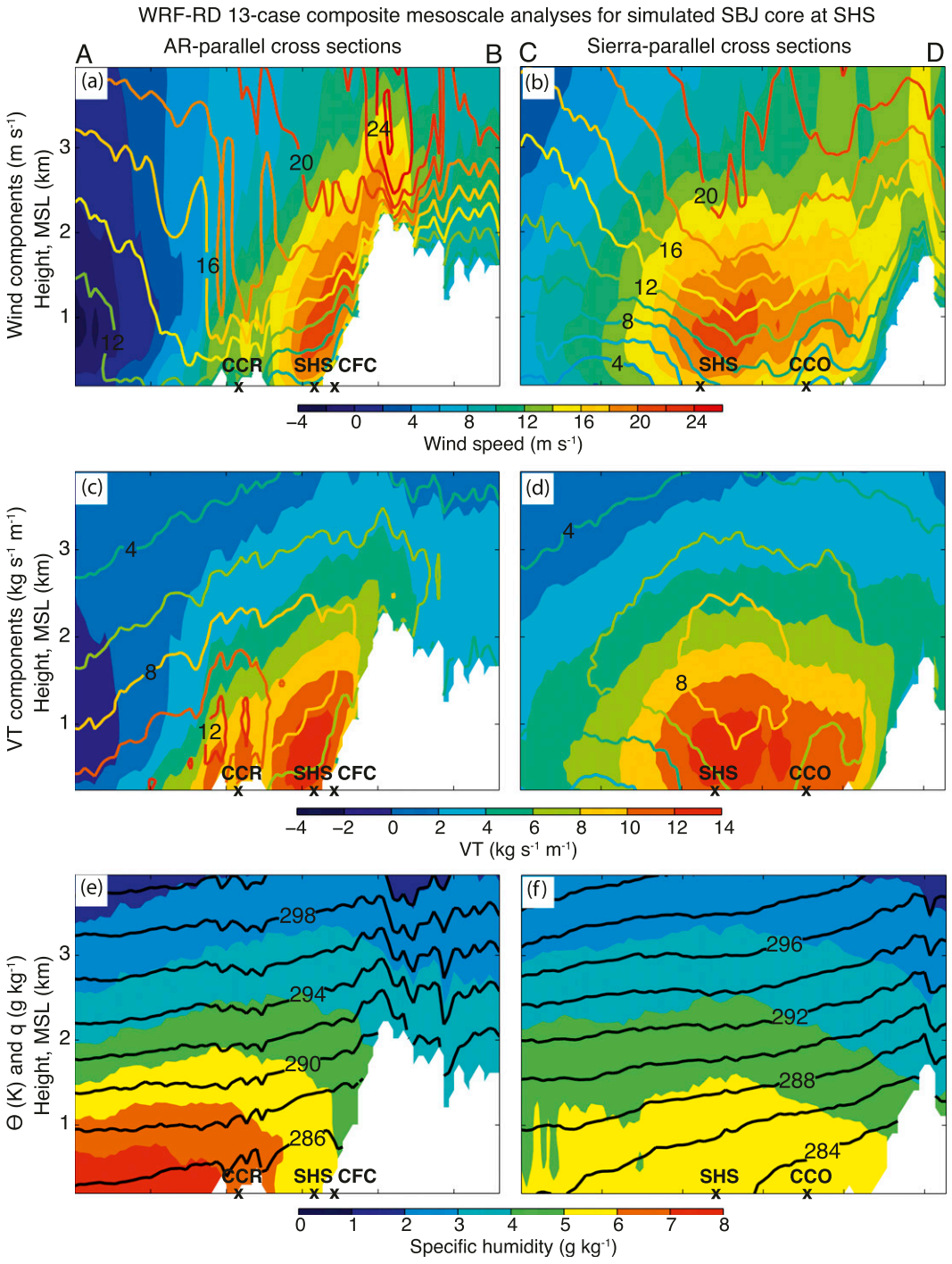

FIG. 12. Composite, 13-case cross-sectional analyses along lines (left) A–B (AR parallel) and (right) C–D (Sierra parallel) in Fig. 10 derived from the WRF-RD gridded dataset for the hour of the simulated SBJ core (i.e., V_{max}) at the grid point closest to SHS: (a) cross section A–B showing AR-parallel isotachs ($m\,s^{-1}$, directed from 220°; color contours) and Sierra-parallel isotachs ($m\,s^{-1}$, directed from 160°; color fill); (b) as in (a), but for cross section C–D; (c) cross section A–B showing VT_{AR} ($kg\,s^{-1}\,m^{-1}$, directed from 220°; color contours) and VT_{SBJ} ($kg\,s^{-1}\,m^{-1}$, directed from 160°; color fill); (d) as in (c), but for cross section C–D; (e) cross section A–B showing θ (K, black contours) and q ($g\,kg^{-1}$; color fill); and (f) as in (e), but for cross section C–D. The grid points closest to the four interior wind profiler sites are marked and labeled.

6. Conclusions

A network of five 915-MHz wind profilers, GPS receivers, and surface sites provided the observational foundation for a composite study of SBJs, ARs, and their interactions over Northern California's CV and adjacent Sierra foothills and coastal zone during multiple cool seasons. To build upon this observational base, two reanalysis datasets were examined to provide additional kinematic and thermodynamic context: the 32-km resolution NARR available at 3-h intervals and the experimental 6-km resolution WRF-RD available hourly. Combined, these observational and reanalysis datasets conform to the basic, terrain-following, structural characteristics of SBJs first observed during SCPP (e.g., Parish 1982; Marwitz 1983, 1987). These datasets also extend the SBJ research results from SCPP, and from those that followed (e.g., Neiman et al. 2010; Hughes et al. 2012; Kingsmill et al. 2013), by providing new insights into the composite spatiotemporal characteristics of the kinematics, thermodynamics, and precipitation across the northern CV and adjacent high terrain. These characteristics are summarized in the conceptual schematic of Fig. 13.

During the six cool seasons between 2005/06 and 2010/11, 65 SBJ cases were tagged at the SHS wind profiler. Given the importance of strong SBJs to the regional hydrometeorology (e.g., Neiman et al. 2010), we chose the 20 strongest cases to composite in a 24-h period centered on the SBJ core. To provide a regionwide observational depiction of the SBJ and associated AR across Northern California, concurrent wind profiler data were also analyzed from the four adjacent profiler sites, but these data were simultaneously available only during the last two cool seasons. Thirteen of the 20 strongest SBJ cases at SHS occurred during these two cool seasons, and the 13-case composite analyses at that site matched the larger 20-case composites. Hence, the SBJ core in the 13 strongest cases from 2009 to 2011 at SHS was used as a temporal anchor for the composite analyses at the other profiler sites.

The observational analyses show shallow, cool, south-southeasterly, Sierra-parallel flow and associated water vapor transport strengthening with time early in the 24-h composite period, culminating in an SBJ core of $>20\,\mathrm{m\,s^{-1}}$ situated less than 1 km above the eastern CV. The SBJ core increases in MSL altitude up the Sierra's windward slope and poleward toward the north end of the CV, but it does not reach the western edge of the CV (Fig. 13), in agreement with the case study results of Kingsmill et al. (2013). Above the developing SBJ, strengthening southwesterly flow descends with time in response to the landfall of an AR. The moistening SBJ reaches maximum intensity during the strongest AR flow aloft. The SBJ subsequently weakens at the back edge of the AR and with the initial cold-frontal period aloft, during which period the shallow flow shifts to southwesterly and the heaviest precipitation falls in the Sierra foothills. An orographic precipitation analysis quantitatively links the Sierra-perpendicular (i.e., nearly AR parallel) flow and associated water vapor transport to enhanced precipitation along the Sierra's windward slope, and it also ties the SBJ-parallel flow and water vapor transport to enhanced precipitation at the north end of the CV (Figs. 13b,c). The altitude of the orographic controlling layer in the Sierra (~1.5 km MSL) is higher than that observed in earlier studies along the California coast (~1 km MSL; Neiman et al. 2002, 2009) because the terrain is higher and the blocked SBJ flow deeper than in the coastal zone. A much shallower orographic controlling layer in the SBJ (~0.75 km MSL) modulates the precipitation at the north end of the CV. Synoptically forced stratiform clouds cover the domain.

From a reanalysis perspective, the NARR provides composite synoptic-scale context during the core period of SBJ conditions, including detailing the landfall of a deep-tropospheric trough, an AR, and upward-motion forcing into Northern California. The companion WRF-RD gridded dataset replicates the wind profilers' fundamental SBJ and AR characteristics observed across Northern California and is, therefore, used to further our understanding of these phenomena. The WRF-RD composite analyses showcase the vertically resolved thermodynamic structures and water vapor transport corridors in the SBJ (situated over the east side of the northern CV and above the Sierra's windward slope) and in the AR (extending inland from the Pacific). Significantly, these analyses also highlight the inland penetration of the AR through the SFB gap. Although the core of the AR-parallel water vapor transport aloft slopes over the SBJ, the AR also contributes to moistening of the SBJ flow as the shallow low-level flow entering the SFB gap turns poleward up the northern CV. The SBJ moistening, in turn, contributes to the static destabilization of the lower troposphere near the trailing edge of the AR and during the onset of cold-frontal cooling aloft. During this period, the winds veer temporally from southerly to southwesterly above the decaying SBJ, thus yielding flow that is directed increasingly perpendicular to the Sierra crest. Combined, these factors create an environment conducive to the orographic enhancement of precipitation along the Sierra's windward slope.

To more efficiently balance the conflicting demands of water storage and flood mitigation in this orographically complex region, it is important to fully understand the relevant physical processes that lead to the generation

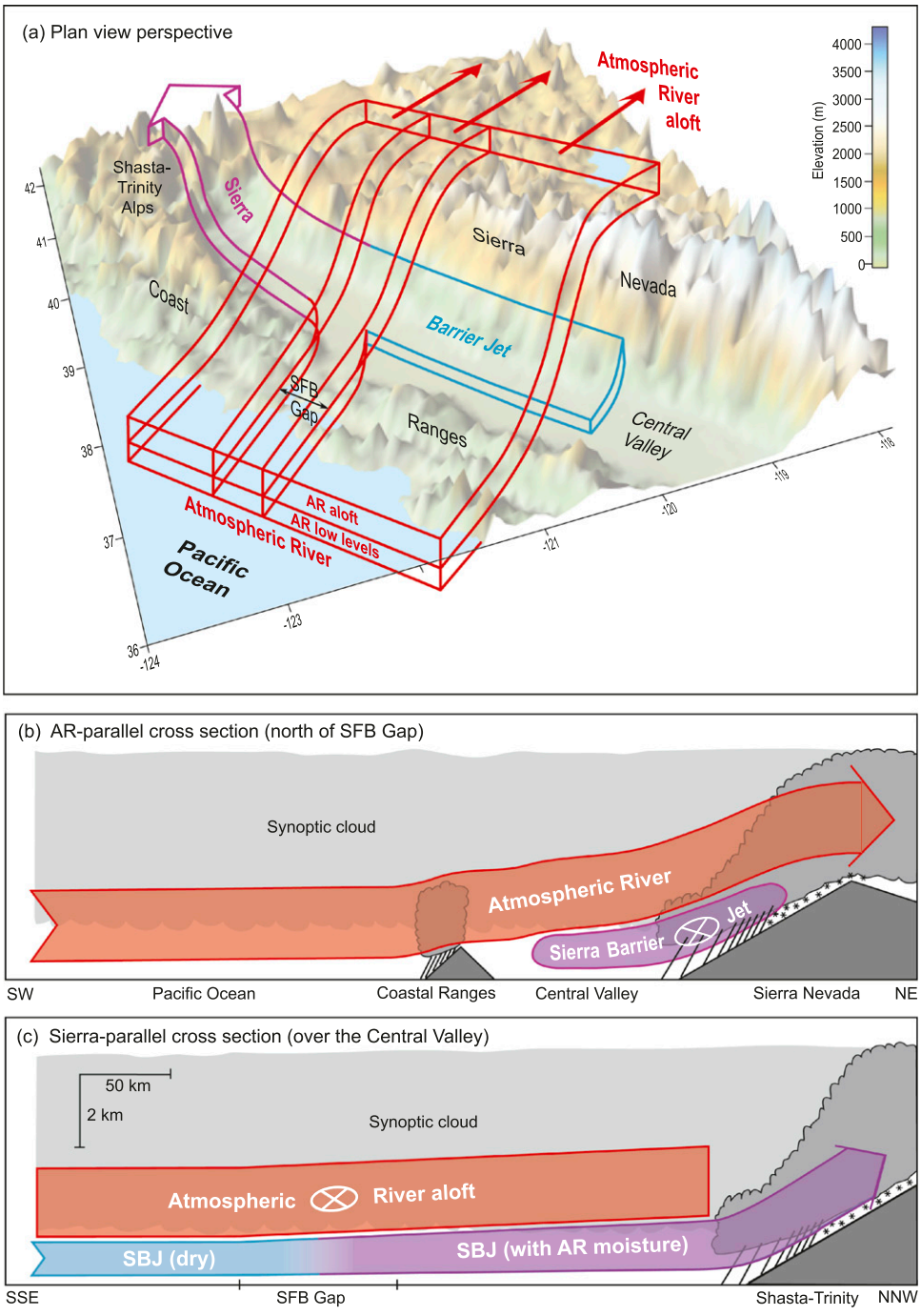

FIG. 13. Conceptual representation of key SBJ and AR characteristics based on the 13-case composite analysis. (a) A 3D plan-view perspective of the SBJ over the CV (blue/purple airstream) and the AR making landfall (red airstream). The shallow SBJ ascends the Shasta–Trinity Alps from the southeast and also slopes up the Sierra Nevada foothills. The upper portion of the AR ascends the SBJ and Sierra Nevada from the southwest, while the lower portion is either rained out along the coast ranges or is funneled through the SFB gap, joins the dry SBJ originating from the southeast (blue), and veers northwestward while adding water vapor to the SBJ over the northern CV (purple). (b),(c) AR- and Sierra-parallel cross-sectional perspectives of the SBJ and AR, respectively [color coding as in (a)]. A schematic representation of the orographically enhanced clouds (medium gray shade, dark outline) and precipitation over the Sierra Nevada, the Shasta–Trinity Alps, and the coast ranges is portrayed, as is the synoptic cloud field (light gray shade). The SBJ deepens poleward of the SFB gap as the low-level portion of the AR contributes to the SBJ airstream there.

and redistribution of heavy precipitation. Both the SBJ and AR significantly impact such processes, and this study has provided key insights into spatiotemporal linkages between these coupled atmospheric features and the precipitation they generate and modulate. Future work will more fully utilize the unique WRF-RD dataset to investigate kinematic and thermodynamic controls on various aspects of SBJs (e.g., strength and altitude), ARs, and their mutual interactions and to more fully assess their impacts on precipitation distributions and amounts.

Acknowledgments. Jim Adams assisted in the electronic drafting of figures. Allen White generated the terrain base map. We appreciate the comments and suggestions by David Reynolds and Allen White of NOAA and by three anonymous reviewers. Their efforts improved the scope and quality of this manuscript.

REFERENCES

Baldwin, M. E., and K. E. Mitchell, 1997: The NCEP hourly multisensor U.S. precipitation analysis for operations and GCIP research. Preprints, *13th Conf. on Hydrology,* Long Beach, CA, Amer. Meteor. Soc., 54–55.

Beebe, R. G., and F. C. Bates, 1955: A mechanism for assisting in the release of convective instability. *Mon. Wea. Rev.,* **83,** 1–10.

Bell, G. D., and L. F. Bosart, 1988: Appalachian cold-air damming. *Mon. Wea. Rev.,* **116,** 137–161.

Bjerknes, J., and H. Solberg, 1921: Meteorological conditions for the formation of rain. *Geofys. Publ.,* **2,** 1–60.

Braun, S. A., R. A. Houze Jr., and B. F. Smull, 1997: Airborne dual-Doppler observations of an intense frontal system approaching the Pacific Northwest coast. *Mon. Wea. Rev.,* **125,** 3131–3156.

——, R. Rotunno, and J. B. Klemp, 1999a: Effects of coastal orography on landfalling cold fronts. Part I: Dry, inviscid dynamics. *J. Atmos. Sci.,* **56,** 517–533.

——, ——, and ——, 1999b: Effects of coastal orography on landfalling cold fronts. Part II: Effects of surface friction. *J. Atmos. Sci.,* **56,** 3366–3384.

Carter, D. A., K. S. Gage, W. L. Ecklund, W. M. Angevine, P. E. Johnston, A. C. Riddle, J. S. Wilson, and C. R. Williams, 1995: Developments in UHF lower tropospheric wind profiling at NOAA's Aeronomy Laboratory. *Radio Sci.,* **30,** 997–1001.

Colle, B. A., and C. F. Mass, 1995: The structure and evolution of cold surges east of the Rocky Mountains. *Mon. Wea. Rev.,* **123,** 2577–2610.

Daly, C., P. Neilson, and D. L. Phillips, 1994: A statistical-topographic model for mapping climatological precipitation over mountainous terrain. *J. Appl. Meteor.,* **33,** 140–158.

Dettinger, M. D., 2004: Fifty-two years of ''pineapple-express'' storms across the west coast of North America. Rep. CEC-500-2005-004, 15 pp. [Available online at http://www.energy.ca.gov/2005publications/CEC-500-2005-004/CEC-500-2005-004.PDF.]

——, K. Redmond, and D. Cayan, 2004: Winter orographic precipitation ratios in the Sierra Nevada—Large-scale atmospheric circulations and hydrologic consequences. *J. Hydrometeor.,* **5,** 1102–1116.

——, F. M. Ralph, T. Das, P. J. Neiman, and D. Cayan, 2011: Atmospheric rivers, floods, and the water resources of California. *Water,* **3,** 455–478.

——, and Coauthors, 2012: Design and quantification of an extreme winter storm scenario for emergency preparedness and planning exercises in California. *Nat. Hazards,* **60,** 1085–1111.

Doyle, J. D., 1997: The influence of mesoscale coastal orography on a coastal jet and rainband. *Mon. Wea. Rev.,* **125,** 1465–1488.

Duan, J. M., and Coauthors, 1996: GPS meteorology: Direct estimation of the absolute value of precipitable water. *J. Appl. Meteor.,* **35,** 830–838.

Durran, D. R., 1990: Mountain waves and downslope winds. *Atmospheric Processes over Complex Terrain, Meteor. Monogr.,* No. 45, Amer. Meteor. Soc., 59–81.

Egger, J., and K. P. Hoinka, 1992: Fronts and orography. *Meteor. Atmos. Phys.,* **48,** 3–36.

Fulton, R. A., J. P. Breidenbach, D.-J. Seo, D. A. Miller, and T. O'Bannon, 1998: The WSR-88D rainfall algorithm. *Wea. Forecasting,* **13,** 377–395.

Galewsky, J., and A. Sobel, 2005: Moist dynamics and orographic precipitation in northern and central California during the New Year's flood of 1997. *Mon. Wea. Rev.,* **133,** 1594–1612.

Guan, B., D. E. Waliser, N. P. Molotch, E. J. Fetzer, and P. J. Neiman, 2012: Does the Madden–Julian oscillation influence wintertime atmospheric rivers and snowpack in the Sierra Nevada? *Mon. Wea. Rev.,* **140,** 325–342.

Heggli, M. R., and R. M. Rauber, 1988: The characteristics and evolution of supercooled water in wintertime storms over the Sierra Nevada: A summary of microwave radiometric measurements taken during the Sierra Cooperative Pilot Project. *J. Appl. Meteor.,* **27,** 989–1015.

Hollinger, J. P., J. L. Peirce, and G. A. Poe, 1990: SSM/I instrument evaluation. *IEEE Trans. Geosci. Remote Sens.,* **28,** 781–790.

Hughes, M., P. J. Neiman, E. Sukovich, and M. Ralph, 2012: Representation of the Sierra Barrier Jet in 11 years of a high-resolution dynamical reanalysis downscaling compared with long-term wind profiler observations. *J. Geophys. Res.,* **117,** D18116, doi:10.1029/2012JD017869.

Kim, J., and H.-S. Kang, 2007: The impact of the Sierra Nevada on low-level winds and water vapor transport. *J. Hydrometeor.,* **8,** 790–804.

Kingsmill, D. E., P. J. Neiman, B. J. Moore, M. Hughes, S. E. Yuter, and F. M. Ralph, 2013: Kinematic and thermodynamic structures of Sierra barrier jets and overrunning atmospheric rivers during a landfalling winter storm in northern California. *Mon. Wea. Rev.,* **141,** 2015–2036.

Lavers, D. A., R. P. Allan, E. F. Wood, G. Villarini, D. J. Brayshaw, and A. J. Wade, 2011: Winter floods in Britain are connected with atmospheric rivers. *Geophys. Res. Lett.,* **38,** L23803, doi:10.1029/2011GL049783.

Lilly, D. K., and E. J. Zipser, 1972: The Front Range windstorm of 11 January 1972: A meteorological narrative. *Weatherwise,* **25,** 56–63.

Loescher, K. A., G. S. Young, B. A. Colle, and N. S. Winstead, 2006: Climatology of barrier jets along the Alaskan coast. Part I: Spatial and temporal distributions. *Mon. Wea. Rev.,* **134,** 437–453.

Lund, J. R., 2007: *Envisioning Futures for the Sacramento–San Joaquin Delta.* Public Policy Institute of California, 285 pp.

Lundquist, J. D., J. R. Minder, P. J. Neiman, and E. M. Sukovich, 2010: Relationships between barrier jet heights, precipitation distributions, and streamflow in the northern Sierra Nevada. *J. Hydrometeor.,* **11,** 1141–1156.

Marwitz, J., 1983: The kinematics of orographic airflow during Sierra storms. *J. Atmos. Sci.,* **40,** 1218–1227.

——, 1987: Deep orographic storms over the Sierra Nevada. Part I: Thermodynamic and kinematic structure. *J. Atmos. Sci.,* **44,** 159–173.

Mattioli, V., E. R. Westwater, C. Cimini, J. S. Liljegren, B. M. Lesht, S. I. Gutman, and F. J. Schmidlin, 2007: Analysis of radiosonde and ground-based remotely sensed PWV data from the 2004 North Slope of Alaska Arctic Winter Radiometric Experiment. *J. Atmos. Oceanic Technol.,* **24,** 415–431.

Mesinger, F., and Coauthors, 2006: North American Regional Reanalysis. *Bull. Amer. Meteor. Soc.,* **87,** 343–360.

Neiman, P. J., F. M. Ralph, A. B. White, D. E. Kingsmill, and P. O. G. Persson, 2002: The statistical relationship between upslope flow and rainfall in California's coastal mountains: Observations during CALJET. *Mon. Wea. Rev.,* **130,** 1468–1492.

——, P. O. G. Persson, F. M. Ralph, D. P. Jorgensen, A. B. White, and D. E. Kingsmill, 2004: Modification of fronts and precipitation by coastal blocking during an intense landfalling winter storm in Southern California: Observations during CALJET. *Mon. Wea. Rev.,* **132,** 242–273.

——, F. M. Ralph, G. A. Wick, Y.-H. Kuo, T.-K. Wee, Z. Ma, G. H. Taylor, and M. D. Dettinger, 2008a: Diagnosis of an intense atmospheric river impacting the Pacific Northwest: Storm summary and offshore vertical structure observed with COSMIC satellite retrievals. *Mon. Wea. Rev.,* **136,** 4398–4420.

——, ——, ——, J. Lundquist, and M. D. Dettinger, 2008b: Meteorological characteristics and overland precipitation impacts of atmospheric rivers affecting the West Coast of North America based on eight years of SSM/I satellite observations. *J. Hydrometeor.,* **9,** 22–47.

——, A. B. White, F. M. Ralph, D. J. Gottas, and S. I. Gutman, 2009: A water vapour flux tool for precipitation forecasting. *Proc. Inst. Civ. Eng. Water Manage.,* **162,** 83–94, doi:10.1680/wama.2009.162.2.83.

——, E. M. Sukovich, F. M. Ralph, and M. Hughes, 2010: A seven-year wind profiler–based climatology of the windward barrier jet along California's northern Sierra Nevada. *Mon. Wea. Rev.,* **138,** 1206–1233.

——, L. J. Schick, F. M. Ralph, M. Hughes, and G. A. Wick, 2011: Flooding in western Washington: The connection to atmospheric rivers. *J. Hydrometeor.,* **12,** 1337–1358.

Pandey, G. R., D. R. Cayan, and K. P. Georgakakos, 1999: Precipitation structure in the Sierra Nevada of California during winter. *J. Geophys. Res.,* **104,** 12 019–12 030.

Parish, T. R., 1982: Barrier winds along the Sierra Nevada Mountains. *J. Appl. Meteor.,* **21,** 925–930.

Pierrehumbert, R. T., and B. Wyman, 1985: Upstream effects of mesoscale mountains. *J. Atmos. Sci.,* **42,** 977–1003.

Ralph, F. M., and M. D. Dettinger, 2012: Historical and national perspectives on extreme west-coast precipitation associated with atmospheric rivers during December 2010. *Bull. Amer. Meteor. Soc.,* **93,** 783–790.

——, P. J. Neiman, and G. A. Wick, 2004: Satellite and CALJET aircraft observations of atmospheric rivers over the eastern North Pacific Ocean during the winter of 1997/98. *Mon. Wea. Rev.,* **132,** 1721–1745.

——, and Coauthors, 2005: Improving short term (0–48 hour) cool-season quantitative precipitation forecasting: Recommendations from a USWRP workshop. *Bull. Amer. Meteor. Soc.,* **86,** 1619–1632.

——, P. J. Neiman, G. A. Wick, S. I. Gutman, M. D. Dettinger, D. R. Cayan, and A. B. White, 2006: Flooding on California's Russian River: The role of atmospheric rivers. *Geophys. Res. Lett.,* **33,** L13801, doi:10.1029/2006GL026689.

——, ——, G. N. Kiladis, K. Weickmann, and D. M. Reynolds, 2011: A multiscale observational case study of a Pacific atmospheric river exhibiting tropical–extratropical connections and a mesoscale frontal wave. *Mon. Wea. Rev.,* **139,** 1169–1189.

Rauber, R. M., 1992: Microphysical structure and evolution of a central Sierra Nevada orographic cloud system. *J. Appl. Meteor.,* **31,** 3–24.

Reeves, H. D., Y.-L. Lin, and R. Rotunno, 2008: Dynamic forcing and mesoscale variability of heavy precipitation events over the Sierra Nevada Mountains. *Mon. Wea. Rev.,* **136,** 62–77.

Reynolds, D. W., and A. S. Dennis, 1986: A review of the Sierra Cooperative Pilot Project. *Bull. Amer. Meteor. Soc.,* **67,** 513–523.

——, and A. P. Kuciauskas, 1988: Remote and in situ observations of Sierra Nevada winter mountain clouds: Relationships between mesoscale structure, precipitation and liquid water. *J. Appl. Meteor.,* **27,** 140–156.

Rhea, J. O., 1978: Orographic precipitation model for hydrometeorological use. Ph.D. dissertation, Dept. of Atmospheric Science Paper 287, Colorado State University, 198 pp.

Schaake, J., A. Henkel, and S. Cong, 2004: Application of PRISM climatologies for hydrologic modeling and forecasting in the western U.S. Preprints, *18th Conf. on Hydrology,* Seattle, WA, 5.3. [Available online at https://ams.confex.com/ams/pdfpapers/72159.pdf.]

Schumacher, P. N., D. J. Knight, and L. F. Bosart, 1996: Frontal interaction with the Appalachian Mountains. Part I: A climatology. *Mon. Wea. Rev.,* **124,** 2453–2468.

Smith, B. L., S. E. Yuter, P. J. Neiman, and D. E. Kingsmill, 2010: Water vapor fluxes and orographic precipitation over northern California associated with a land-falling atmospheric river. *Mon. Wea. Rev.,* **138,** 74–100.

Smith, R. B., 1979: The influence of mountains on the atmosphere. *Advances in Geophysics,* Vol. 21, Academic Press, 87–230.

Smolarkiewicz, P. K., and R. Rotunno, 1990: Low Froude number flow past three-dimensional obstacles. Part II: Upwind flow reversal zone. *J. Atmos. Sci.,* **47,** 1498–1511.

Smutz, S. W., 1986: A climatology of the Sierra Nevada barrier jet. M.S. thesis, Paper AS-153, Dept. of Atmospheric Science, University of Wyoming, 108 pp.

Steiner, M., O. Bousquet, R. A. Houze, Jr., B. F. Smull, and M. Mancini, 2003: Airflow within major Alpine river valleys under heavy rainfall. *Quart. J. Roy. Meteor. Soc.,* **129,** 411–431.

Stohl, A., C. Forster, and H. Sodemann, 2008: Remote sources of water vapor forming precipitation on the Norwegian west coast at 60°N—A tale of hurricanes and an atmospheric river. *J. Geophys. Res.,* **113,** D05102, doi:10.1029/2007JD009006.

Viale, M., and M. N. Nuñez, 2011: Climatology of winter orographic precipitation over the subtropical central Andes and associated synoptic and regional characteristics. *J. Hydrometeor.,* **12,** 481–507.

Weber, B. L., D. B. Wuertz, D. C. Welsh, and R. McPeek, 1993: Quality controls for profiler measurements of winds and RASS temperatures. *J. Atmos. Oceanic Technol.,* **10,** 452–464.

Yu, C.-K., and B. F. Smull, 2000: Airborne Doppler observations of a landfalling cold front upstream of steep coastal orography. *Mon. Wea. Rev.,* **128,** 1577–1603.

——, and N. A. Bond, 2002: Airborne Doppler observations of a cold front in the vicinity of Vancouver Island. *Mon. Wea. Rev.,* **130,** 2692–2708.

Zhu, Y., and R. E. Newell, 1998: A proposed algorithm for moisture fluxes from atmospheric rivers. *Mon. Wea. Rev.,* **126,** 725–735.